Natural Resources Research, Vol. 34, No. 4, August 2025 (© 2025)
https://doi.org/10.1007/s11053-025-10483-0

Review Paper

From Rock to Fiber: The Mechanical Properties of Continuous Rock Fibers

Yixuan Ma,[1] Zeshi Guo,[2,3] Jimin Fu,[1] Xiongyu Xi,[2,3] Pengcheng Ma,[2,3] and Xungai Wang[1,4]

Received 4 December 2024; accepted 5 March 2025
Published online: 15 April 2025

The mechanical properties of continuous rock fiber (CRF), particularly its elastic modulus and tensile strength, are essential requirements for the ever-increasing applications of this material. Studies on CRF have primarily focused on its application in fiber-reinforced composites, with much less emphasis on the analysis of the fiber structure–property relationship. This review summarizes and discusses the current experimental approaches, theories, models, and parameters in different production stages (geochemistry, rock screening, melting, cooling, and fiber drawing) that would affect the elastic modulus and tensile strength of CRF. For the current research results, the general debate is the trade-off between the network structure and defects in the tensile strength of CRF. The study of elastic modulus functions as the fundamental of tensile strength, as the former can be explored regardless of certain defects, only considering the microstructure of the network, local atom coordination and bonding, whereas the latter can be studied beyond characterizing the defects. The limitations of current methods include theories for crystals and stable substances, which may not be applicable to metastable monofilaments or complex CRF glasses. Experimentally, in situ testing is difficult for fibers in certain procedures that cause permanent damage. Machine learning (ML) and molecular dynamics (MD) can compensate for the lack of experimental data, reduce the effects of operational procedures, provide structure-based information, and reflect the combined effects of multiple input features. An ongoing approach should be based on a solid understanding of conventional models and improvements in standardized experimental and MD datasets incorporated with ML methods.

KEY WORDS: Continuous rock fiber, Basalt, Mechanical properties, Elastic modulus, Tensile strength.

[1]Joint Research Center for Fiber Innovations and Renewable Materials, The Hong Kong Polytechnic University, Hung Hom, Kowloon 999077, Hong Kong, China.
[2]Laboratory of Environmental Science and Technology, The Xinjiang Technical Institute of Physics and Chemistry, Key Laboratory of Functional Materials and Devices for Special Environments, Chinese Academy of Sciences, Urumqi 830011, China.
[3]Center of Materials Science and Optoelectronics Engineering, University of Chinese Academy of Sciences, Beijing 100049, China.
[4]To whom correspondence should be addressed; e-mail: xungai.wang@polyu.edu.hk

INTRODUCTION

Rock fibers (RFs), including short rock fibers (SRFs) and continuous rock fibers (CRFs), are made from basaltic and andesitic rocks including basalt, basalt andesite and andesite. RFs have been commonly cited as ''basalt fiber'' in previous studies, although the rocks used contain different chemical compositions that are not limited to basalt. This review uses the term ''rock fiber'' instead of ''basalt

fiber,'' as proposed by Ersoy et al. (2021). The rocks are made into amorphous fibers through a melt-spinning process. CRF is suggested to have better mechanical properties than SRF, better thermal and chemical resistance than glass fiber (GF), and a lower price than carbon fiber (CF) (Ivanitskii & Gorbachev, 2011). CRF has been widely used in RF-reinforced composites (RFRC) in the civil engineering, automotive, defense, and space industries. As a high-performance fiber that can be made from ample resources on the Earth, Moon (Guo et al., 2022a), and Mars (Guo et al., 2024), CRF is significant for researchers, investors, governments, and humanity exploring the universe (Ersoy et al., 2021).

A general search of articles from the earliest to 2024 in Scopus and IEEE using Boolean operators with the keywords basalt AND fiber and continuous AND basalt AND fiber is summarized in Figure 1, indicating a growing research interest in RF with a growing number of articles. Although research on RF began approximately a century ago (Dhé, 1923), studies on RFRC account for more than half of the total research output, with CRF receiving comparatively less attention. The mechanical properties of CRF, including the elastic modulus and tensile strength, are essential requirements for industrial applications. A ''high-performance CRF,'' according to the standard GBT/T38111, should have an elastic modulus of over 90 GPa and tensile strength of over 2500 MPa. Only a very limited amount of CRF can meet the requirements of ''high-performance CRF,'' which hinders its claimed superiority over GF and CF. Owing to the complicated composition of this natural material, current research has not reached an agreement on a widely applicable measure for improving the CRF properties. Comprehensive reviews have been conducted on RF history and production techniques (Jamshaid & Mishra, 2016), RF applications (Jamshaid, 2017), RFRC (Dhand et al., 2015; Fiore et al., 2015), and RFRC in specific matrices, such as polymers (Vinay et al., 2022) and concrete (Al-Rousan et al., 2023). However, a review of the mechanical performance of CRF is unavailable in the literature.

This review covers studies on the mechanical properties of CRF, including an overview of the current experimental and theoretical research approaches. Parameters affecting the elastic modulus and tensile strength of the CRF span from the rock screening to the melting and fiber drawing stages. Each stage influences the parameters of the subsequent stages and the ultimate CRF performance. In principle, the established theories for crystals and stable substances may not be directly applicable to monofilament glass owing to their metastable nature. This situation is further complicated by the complex composition of natural basaltic and andesitic rocks, making it even more challenging to analyze. Experimentally, the effects of iron content, fiber diameter, and alkaline components on the mechanical properties of CRF are still debated and require further exploration. Therefore, machine learning (ML) and molecular dynamics (MD) approaches have been proposed to compensate for the lack of experimental data, reduce the effects of operational procedures, provide structure-based information, and reflect the combined effects of different input features. This review will benefit future studies on the basic material properties of basaltic and andesitic rocks for producing high-performance CRF.

RESEARCH APPROACHES

Traditional Theoretical Approaches

CRF is a silicate glass whose structure is commonly explained by a continuous random network model (Zachariasen, 1932). The silica–oxygen tetrahedrons are connected through bridging oxygen (BO) forming rings in different sizes like a ''network.'' The other oxygens are defined as no-bridging oxygen (NBO) (Fig. 2a), with short-range order remaining and almost no long-range order. The structure of the silica tetrahedron network is described using Q^n, where n is the number of BO, including nesosilicate (Q^0), sorosilicate (Q^1), inosilicate (Q^2), phyllosilicate (Q^3), and tectosilicate (Q^4), reflecting different degrees of polymerization. A network former (NF) and network modifier (NM) were used to address the roles of different chemical components. The silica tetrahedron is the main NF, whereas the alkali metals are NMs. Aluminum (Al) and iron (Fe) are mediators that can be either NF or NM. The concentration of alkali metals also influences their impact. The crystal mineral phases in the rock mainly include nesosilicates, inosilicates, and tectosilicates (Fig. 2b). The crystal structures are destroyed upon melting. Following the rapid cooling and drawing processes, the melt solidifies into the CRF, exhibiting an amorphous glass structure. A compact structure with more NF and BO leads to a more polymerized structure, whereas the existence

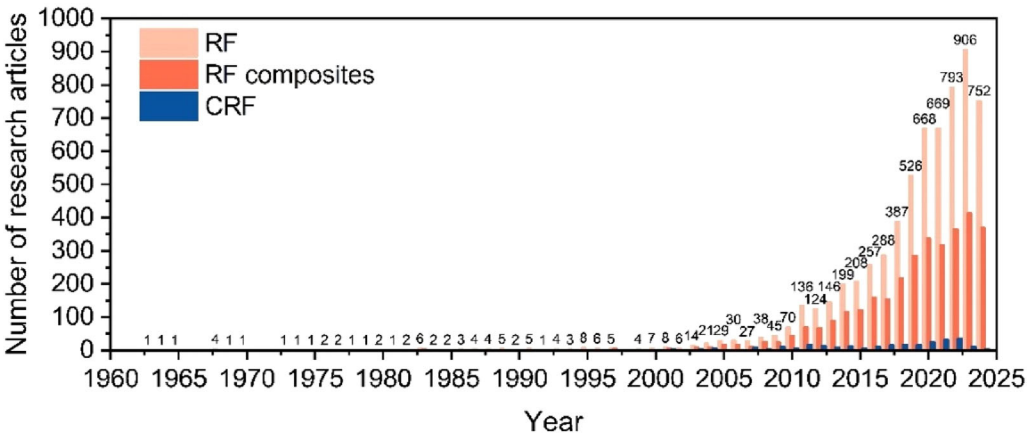

Figure 1. Overview of Scopus and IEEE research articles until 2024 on RF, RF composites and CRF.

of NM breaks some of the Si–O bonds and reduces the number of BO. Deák & Czigány (2009) and Liu et al. (2020b) suggested that an increase in NF strengthens the network and results in better CRF mechanical properties. The positive effects of BO on tensile strength (Gutnikov et al., 2019) and of tectosilicate on the elastic modulus (Gutnikov et al., 2021) have been reported. However, an appropriate amount of NM cations (Kuzmin et al., 2017) and the addition of an aluminosilicate structure (Xing et al., 2019) have also been found to enhance the mechanical properties of CRF. In general, a CRF with a more compact network with better network connections is more likely to exhibit better mechanical properties.

Numerical models based on statistical and physical principles have been applied using two approaches. The first approach involves various stages of CRF production. In the melting stage, the Arrhenius equation (Arrhenius, 1889) and the Vogel–Fulcher–Tammann (VFT) formula (Vogel, 1921; Fulcher, 1925) were commonly used to describe the viscosity–temperature relationship of glass. An empirical formula was established by Meng et al. (2021) to calculate the viscosity of basaltic melt. Numerical models of the fiber drawing process (Yan & Yan, 2004; Kim et al., 2013) have been proposed based on the mass, force, energy, and momentum balance, revealing the effects of the production parameters on the fiber properties. The second approach is based on the CRF end-product, which describes the performance of the fiber. Models such as Makishima–Mackenzie (MM) (Makishima & Mackenzie, 1973; Makishima & Mackenzie, 1975), Rocherulle (Rocherulle et al., 1989; Umar & Ibrahim, 2020), and bond compression and ring deformation (Abd El-Moneim, 2001) models have been used to predict the Young's modulus of silica glass (Yang et al., 2019). Shebanov et al. (2022) applied the Maxwell model (Lamb, 1978) to explain the viscoelasticity of basalt, glass, and aramid fibers. As CRF is a brittle material, Griffith's theory (Griffith, 1921) was used to explain its failure mode and the correlation with tensile strength. The microstructure of silicate glass is usually described by the partial radial distribution function (PDF), radial distribution function (RDF), bond angle distribution (BAD), and coordination number. The PDF and RDF reflect the short-range order of high-entropy alloys such as $Cu_{50}Zr_{50}$ (Yang et al., 2021) and silica melts such as quartz (Mysovsky & Paklin, 2023).

Figure 2c summarizes these theoretical approaches. A comprehensive model for the cooling and glass formation of CRF and glass materials is lacking, presenting an ongoing challenge in the field of amorphous matter research. Regarding the current model, the first approach contains mature physical principles that can explain properties at a specific stage. However, there is a lack of continuity in connecting the different stages, which makes it difficult to draw a coherent conclusion on the ultimate structure of the CRF. The second approach provides certain trends in the structure–property relationship but lacks validation of the proposed microstructure in the experiment. Makishima and Mackenzie (1973) mentioned that ''the exact prediction of the Young's modulus of glasses is a very difficult problem because their structures are not

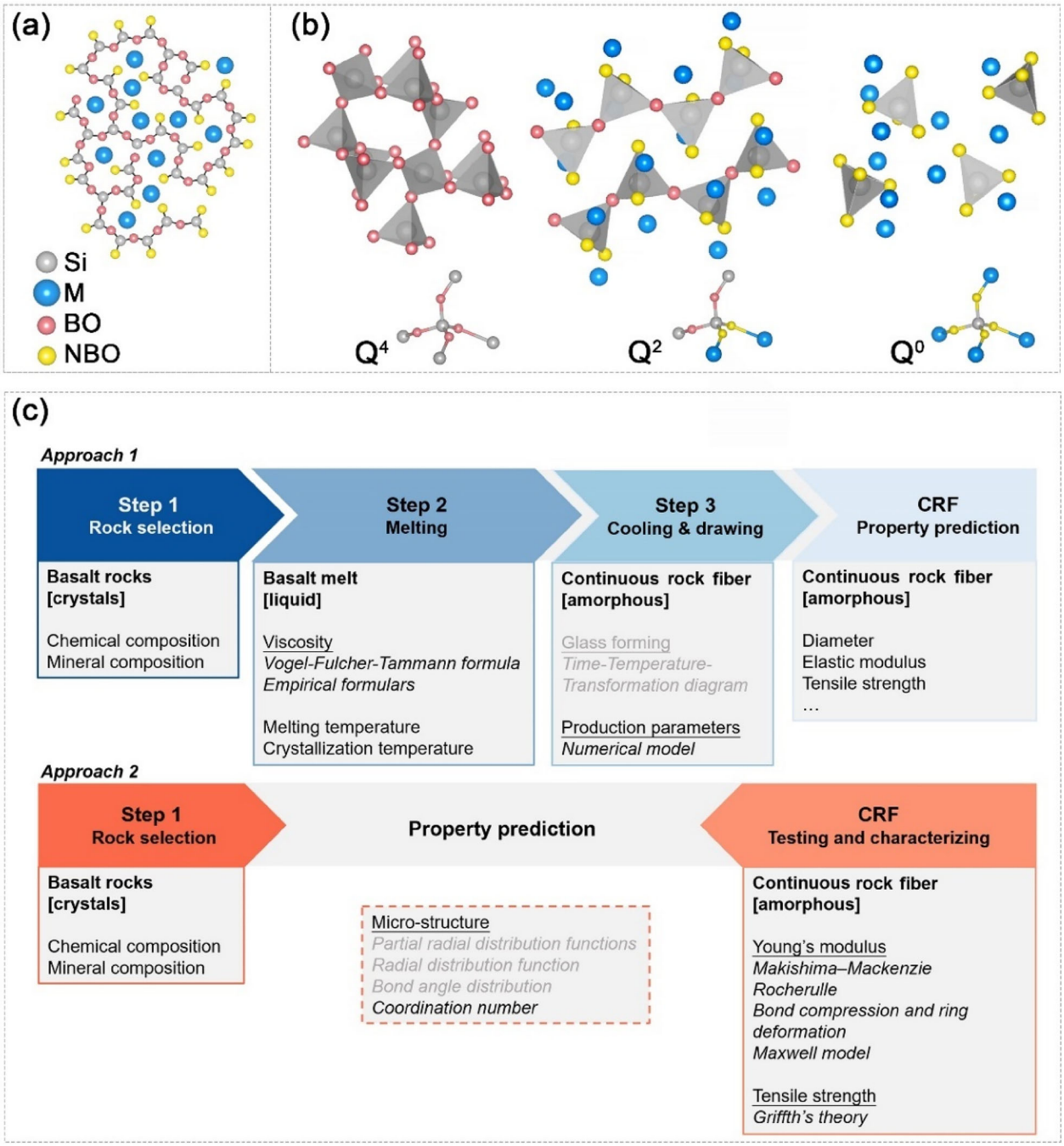

Figure 2. (**a**) Schematic diagram of the atomic arrangement in silicate glass. M represents metal atoms including Fe, Mg, Ca, Na, and K. (**b**). Silicate structure examples with quartz as tectosilicate (Q^4), diopside as inosilicate (Q^2), forsterite as nesosilicate (Q^0). (**c**). Summary of the theoretical approaches in understanding the property–structure relationship of CRF. The text in black covers the theory used in CRF, whereas that in light gray shows the theory used in other amorphous materials but is not widely applied in explaining CRF properties.

quantitatively definable, as for crystalline solids.'' Furthermore, theories typically applied to crystals and stable substances, such as energy minimization, have limited applicability in explaining amorphous states owing to the metastable nature of glass materials.

Experimental Approaches

As shown in Figure 3a, among the 276 articles that studied CRF properties, over one-third focused on tensile strength, followed by heat and alkali resistance, whereas less than 5% examined the elastic modulus. Some properties are interrelated, such as the tensile strength, heat resistance, and crystallization, as they affect each other. The parameters examined from the initial rock state to the molten form, as well as the resulting fiber characteristics (Fig. 3b). Approximately half of the studies focused on the surface treatment and sizing of the fiber, followed by the basalt melt and glass. The effects of the chemical and mineral components of rocks account for approximately 20% of published literature. Studies on production parameters such as nozzle size and fiber drawing speed remain limited. Among the chemical components, two network mediators, iron and aluminum, have been the most studied. In addition to simply considering the chemical compounds, parameters such as the acid modulus (M_a), viscosity modulus (M_v), and NBO divided by the total oxygen (NBO/T) were investigated.

A typical research approach involves examining and contrasting various factors, such as the mineral composition of rock samples from diverse locations. This approach also includes altering the percentage by weight through the addition of chemical substances, combining different rock types, or subjecting the samples to reduction and oxidation processes. The resultant fiber properties are mapped using statistical methods to observe the effect (Ersoy et al., 2022), which covers part of the variables in a discrete form. Statistical methods, such as the response surface methodology (RSM) (Gutnikov & Lazoryak, 2019), have been used to analyze the results, covering the effect of three or more variables. The limitation of the experimental approach lies in the difference in measurement standards, which causes inconsistencies in the results. The experimental procedure is particularly challenging for CRF production owing to the high temperature required and the difficulty in stabilizing the fiber-drawing process. The time spent conducting crossover experiments is another concern, particularly when the variables include over seven chemical compositions, undefined mineral compositions, and parameters in the corresponding production procedures. Conducting certain measurements on a fiber becomes challenging when its diameter ranges from approximately 6 to 20 μm. To address this issue, researchers have either pulverized the fibers into powder form or examined them in bundles. However, these methods introduce additional imprecision as the in situ testing is required when studying the microstructure–property relationship, which is difficult for certain experimental procedures that cause permanent damage to the fiber.

Molecular Dynamics (MD) Approach

MD is based on the analysis of interactions between molecules, and it has been used to study glass structures. MD datasets have been found to have lower noise level than experimental data (Yang et al., 2019). This is one way to compensate for the lack of experimental data and the differences in experimental procedures and standards. Classical MD simulations are based on Newton's second law, which calculates the positions of atoms under various external conditions. The results are highly dependent on the accuracy of the empirical force fields (potentials). A system with complex composition makes it difficult to obtain an accurate force field. Commonly used force fields are Buckingham for silica glass (Hu et al., 2020; Zhang et al., 2024) or Born Mayer Huggins for the melt (Rai & Mountjoy, 2014; Zhang et al., 2024). Wang (2021) used MD to study the elastic modulus of basalt glass with 6000 atoms and simulated three kinds of rocks with different chemical components, which showed a good agreement to the experiment result. The effects of the packing density, coordination number, bonding angle, and ring size on the elastic modulus were preliminarily analyzed. Guo et al. (2023) studied the fiber-forming process using MD along with neutron scattering and Raman spectral experiments. In general, very little research has been published on the MD studies of basalt glass or CRF.

MD has the advantage of providing input features that are difficult to measure or quantify experimentally, such as the atomic packing density, angle distribution, ring size distributions of the NFs, and the average coordination number and bond length of cations on disordered materials (Kobayashi et al., 2023). A common limitation of MD, on the other hand, is the computer intensity required to enable extensive simulations. Calculations based on the *ab initio* method require intensive computer usage, whereas classical force fields are rarely sufficiently accurate to fully describe structural varia-

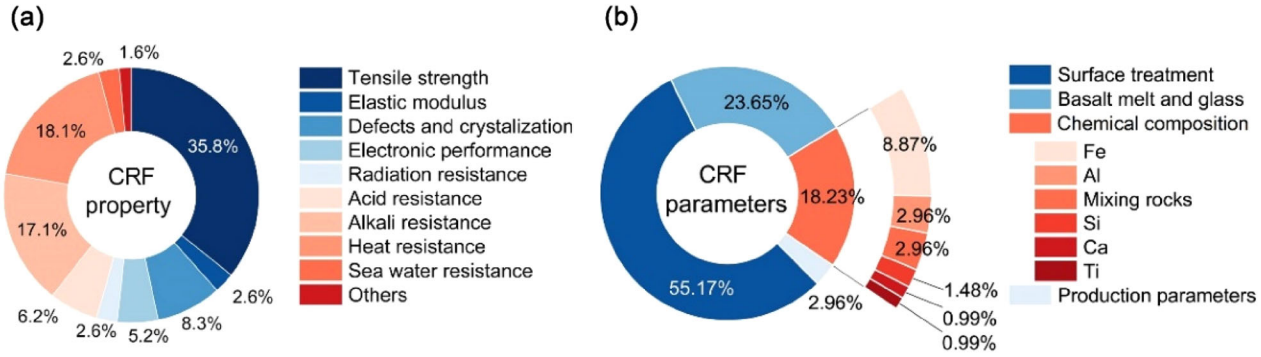

Figure 3. Overview of research area under (**a**) CRF property and (**b**) parameters that would affect CRF performance.

tions in the amorphous state. An additional challenge for MD is dimensionality, which has yet to be aligned with the experimental conditions. Advanced MD models with the help of deep learning (DL) can reach approximately 17 billion atoms (Guo et al., 2022b). While reaching the quasi-static stretching result of CRF at the macroscale, it would require the atom number to exceed approximately 10^{16} – 10^{17}, which is far beyond the current simulation capability. For instance, the simulated elastic modulus is the transient modulus, which is generally higher than quasi-static stretching, but might be closer to the result of the impulse ultrasonic method or dynamic mechanical analysis (DMA). Other options include nanoindentation with a compression depth of approximately 10–40 nm for the transient modulus, such as in metallic glass (Liu et al., 2024) and silicate glass (Ding et al., 2023), and micropillar compression, which has been used in amorphous aluminum oxide (Frankberg et al., 2023). However, it is easier to apply nanoindentation and DMA to bulk materials, but difficult to apply to a single fiber due to the difficulty in clamping and applying unified fiber pretension on different samples.

Machine Learning (ML) Approach

Artificial intelligence (AI) models have been used to predict material performance, guide chemical synthesis, identify new materials, and study the microstructures of materials, along with MD simulations. The combination of big data and AI is called the ''fourth paradigm of science'' (Agrawal & Choudhary, 2016; Butler et al., 2018), which is typically suitable for studying the structure–property correlation of glass materials (Yang et al., 2021). The common ML approach includes factor identification, data mining, feature engineering, training of model with tuned hyperparameters, and validation. A general search in Scopus using the KEYwords ''basalt AND fiber AND machine learning'' and ''basalt AND fiber AND neural network'' revealed 94 articles (Fig. 4a). AI was first used in RF in 2009 and has gradually been applied to predict the properties of RFRC with concrete (Kavya et al., 2022; Rahman & Al-Ameri, 2022) or polymer (Rahman & Al-Ameri, 2021; Najjar et al., 2022) matrices. As shown in Figure 4b, models, such as artificial neural network (ANN), random forest (RF), and support vector regressor (SVR), were primarily used to predict RFRC parameters, such as tensile or compressive strength (Li et al., 2022), based on Python or MATLAB (Kamane et al., 2021; Kim & Oh, 2021; Rahman & Al-Ameri, 2022).

Two articles in 2023 and 2024 used ML to predict the tensile strength and elastic modulus of CRF (Fig. 4a). Zhang et al. (2023) predicted the tensile strength of CRF by comparing models, including decision tree, kernel ridge regression, multivariable linear regression, SVR, RF, and k-nearest neighbors, based on 121 data points collected from the literature with chemical composition and physics-informed descriptors, including Ma and NBO/T. The k-nearest neighbors showed the best performance with a tested R^2 of 0.711. Wang et al. (2024) used a physical-informed neural network (PINN), which incorporated the MM and Rocherulle models into the ANN model to predict the Young's modulus and tensile strength of CRF. The predicted elastic modulus results for 84 samples are shown in Figure 4c. Compared to the model without physical

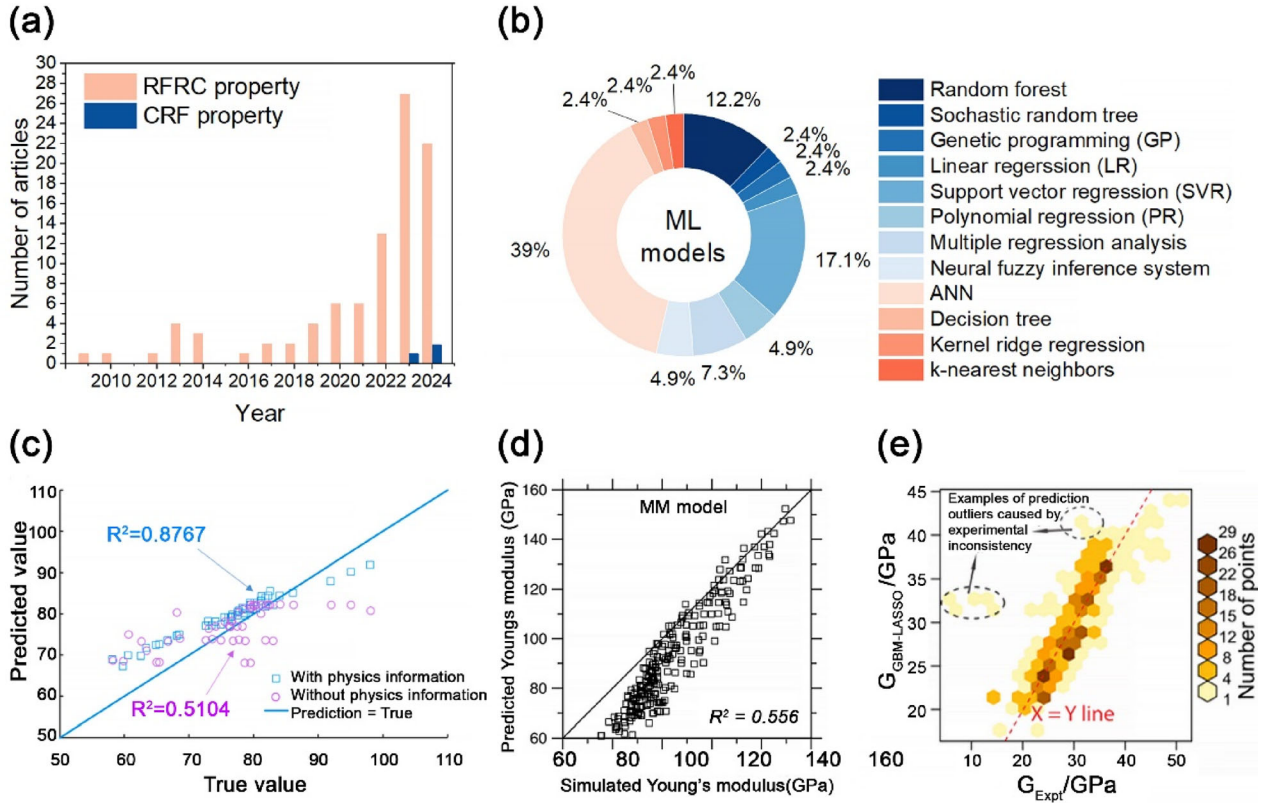

Figure 4. (**a**) Overview of articles from Scopus about RFRC, CRF, and ML. (**b**) ML models used in the research articles. (**c**) Comparison of Young's modulus predicted by ANN with and without physics information (Wang et al., 2024). (**d**) Comparison between the Young's modulus predicted by the MM model and computed by MD simulations (Yang et al., 2019). (**e**) Shear modulus predicted by the GBM–LASSO model ($G_{GBM-LASSO}$) and validated with experimental results (G_{expt}). The dashed-line circles mark out typical examples of prediction outliers caused by experimental data inconsistency (Hu et al., 2020).

information, those with physical principles showed better accuracy with R^2 of 0.8877 and 0.8145 for the training datasets on elastic modulus and tensile strength, respectively. A faster convergence of the PINN model compared to the model without physical information showed the advantage in the model training process. Moreover, Han et al. (2024) used the RF and gradient boosting decision tree to predict the melt viscosity with inputs of temperature and oxide composition of the basalt rocks, with R^2 of the models remaining around 0.98. The interpretable ML model with Shapley additive interpretation (SHAP) provided quantitative insights into the combined effects of chemical composition on viscosity. The above studies have shown the possibility of including physical descriptors and principles in the ML model and provided the first attempts to apply the ML method to predict the mechanical properties of CRF with relatively good accuracy.

Although research using ML and MD in CRF is limited, insights can be gained from studies on other amorphous materials, including property prediction (Hu et al., 2020) and defect identification (Milardovich et al., 2021; Ciarella et al., 2023) for silica glass and amorphous alloys (Galimzyanov et al., 2023). Yang et al. (2019) created a dataset of 231 $CaO–Al_2O_3–SiO_2$ glass samples using high-throughput MD simulations. The research compared polynomial regression, the least absolute shrinkage and selection operator (LASSO), RF, and ANN models, which confirmed that an ANN model with one hidden layer was the most accurate, with R^2 of 0.98 and 0.975 for the training and test datasets, respectively. The model was compared with the conventional MM model, and it was concluded that the MM model underestimated the elastic modulus, particularly in the low-modulus region (Fig. 4d). Hu et al. (2020) combined MD and ML to predict the

elastic modulus of a glass system with more than 10 additive oxides besides SiO_2. The study used the gradient boosting machine (GBM)–LASSO model based on 498 glass compositions in 11 binary and 20 ternary SiO_2-based systems. The model was validated using 550 shear modulus and 1010 elastic modulus data points, which yielded $\sim 90\%$ predictions with relative errors $< 15\%$ for both properties. The authors pointed out the inconsistency between the experimental data gathered from different sources, which affected the accuracy of the validation, as indicated by the circles in Figure 4e. Deringer et al. (2018) used ML potentials in MD to study amorphous silicon in a system with 4096 atoms, which successfully reproduced the first sharp diffraction peak in the experiment. The training database used density function theory results, and the trained potential was used for the MD simulation. The team simulated the structural transition of disordered silicon using 100000 atoms in a later study (Deringer et al., 2021), which showed the advantage of the ML potential. In addition to using chemical components or MD inputs, other sources, such as Raman spectrum data (LaDouceur et al., 2024), were used as input features to study the glass structure.

The studies mentioned above revealed several limitations of using ML. First, the database is yet to be well established, and the experiments lack standardization, raising concerns regarding reproducibility and error propagation (Butler et al., 2018). Existing basaltic rock databases such as those in RF & Composite Materials Technology Development Co., Ltd. (Osnos, 2016), and Xinjiang Technical Institute of Physics and Chemistry, Chinese Academy of Science in China (Xing et al., 2019) are not open to the public. Open-source datasets, such as Mat Web (*Metal, Plastic, and Ceramic Search Index,* n.d., 2024) and EARTHCHEM (EarthChem, 2023), cover the location and chemical and mineral components of rocks, but are usually incomplete. ANN and DL require large datasets for model generalization and accuracy. Datasets with fewer than 100 samples may be insufficient. For PINN, the accuracy of the model is affected by the incorporated physical principles, whereas current models, such as MM, show limitations in considering the metastable nature of glass and using the dissociation energy and packing density of ions as replacement of Madelung constant in crystals, as the actual regulation in the microstructure of glass remains unknown. Second, the current features used in CRF performance prediction are mainly chemical components and parameters, such as NBO/T. The production parameters, which are suggested to affect 30–35% of fiber performance (Osnos, 2016), were not included. The production parameters can be reflected in the diameter and density of the fiber; however, this relationship is not included in the ML features. The thermal history and homogenization time of the different studies also varied. Although the glass structure was assumed homogeneous, variations in the initial stage of the melt affected the ultimate glass structure. Third, a common limitation of ML is its lack of explainability. The SHAP post-analysis method and partial dependence values reflected the positive or negative effects of each parameter on the target feature. However, explaining the underlying structural changes requires input from the microstructure, which is currently experimentally limited by characterization methods. The accuracy of the MD simulated structure has yet to be verified.

The combination of ML and MD compensates for these limitations. MD can provide an enormous database with controlled thermal history. The simulation can fill in incomplete data and include undiscovered data. It also provides diverse information for ML studies. The ML-trained potential improves the accuracy and efficiency of the MD model. Based on physical theories, ML calculations of the MD potential may provide insights into the underlying relationship between the glass structure and its mechanical properties. Involving the traditional theoretical model also improved explainability. As a multicomponent amorphous structure, MD and ML approaches may help gain more knowledge of CRF performance.

CRF PRODUCTION AND ITS MECHANICAL PROPERTIES

Overview of CRF Production Process in Laboratory and Industrial Scales

Typically, the CRFs used in research are purchased from commercial suppliers or drawn from laboratory setups. Like GF, the production process in both laboratories and industry involve preparation, melting, drawing, sizing, and winding (Fig. 5). A pre-melting step is common in laboratory-scale production using fine-ground rock powders passing through 200 mesh sieves for better homogenization. The washed and ground rocks are molten and

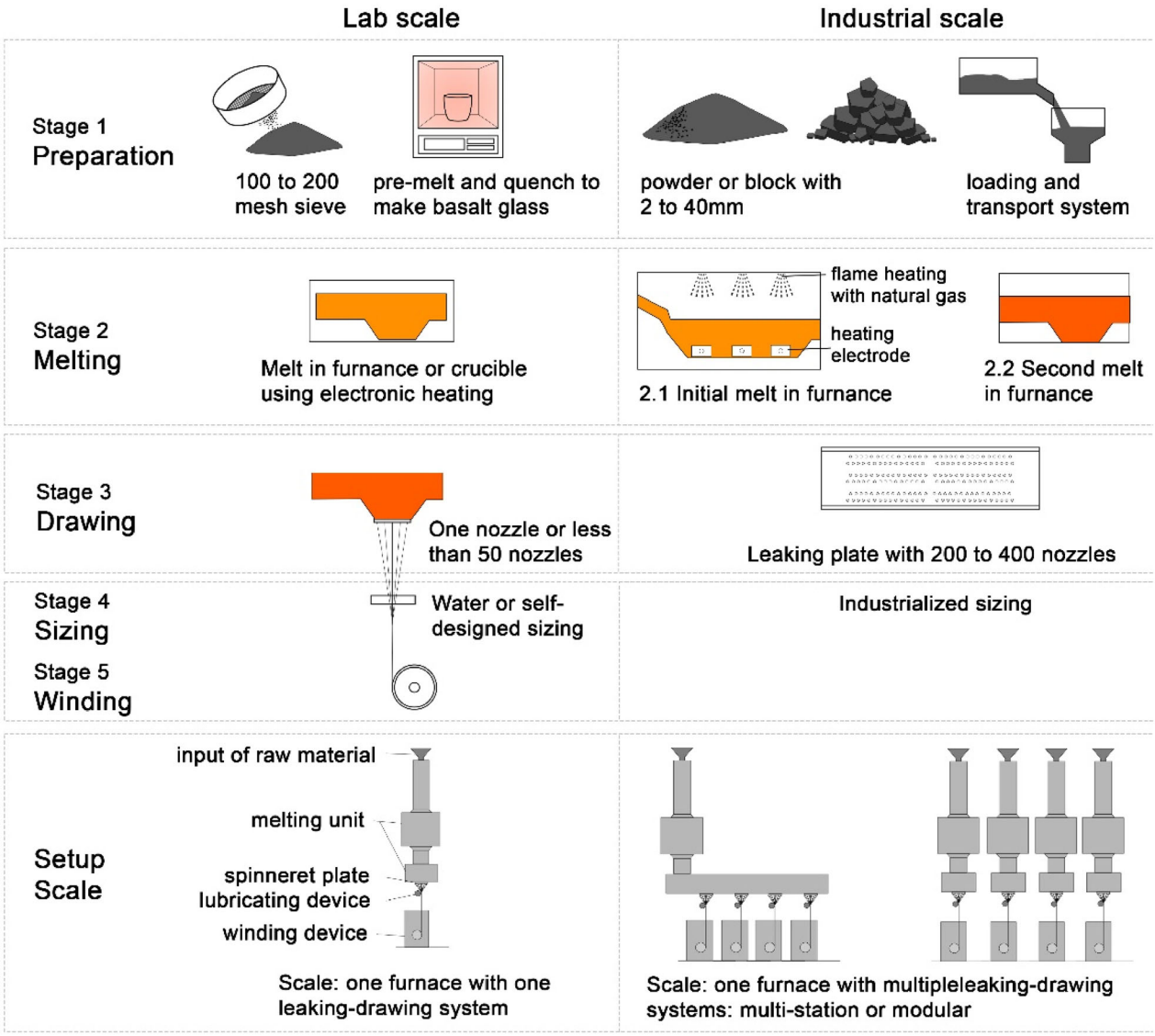

Figure 5. Production of CRF on a laboratory and industrial scale.

quenched into basalt glass balls and then placed in crucibles to undergo the second melting stage. The blocks or powders are directly melted in an industrial production line. The furnace size and heating method depend on the production scale. Electronic heating is used in crucibles and small furnaces in the laboratory setting. On an industrial scale, large furnaces may incorporate multiple fiber-drawing plates (Continuous Basalt & Glass Fibers and Applications (IBE), 2019) and utilize various heating methods, including electronic heating, natural gas flame heating, or a combination of both. In the industry, rocks are first melted at approximately 1500 °C and held for homogenization. The melt is then guided into a smaller furnace to control the fiber drawing temperature accurately. Spinnerets with multiple orifices or nozzles are generally used to produce CRF in laboratories and industry (Deák & Czigány, 2009). After drawing, the fibers undergo a sizing procedure to apply epoxy resin or lubricants on the fiber surface. The fibers are then collected into bundles and pass through the winding stage to form the final product before application.

Table 1. Chemical components of a typical basalt rock (weight percentage%)

SiO_2	Al_2O_3	CaO	Na_2O	K_2O	TiO_2	$FeO + Fe_2O_3$	MgO
55.6	15.8	9.2	2.2	1.8	1.1	10.5	3.7

The difference between laboratory and industrial CRF production is not limited to the production scale. The stability of fiber drawing is crucial. Drawing fiber from fewer nozzles in a laboratory is more manageable than drawing fiber from industrial ones with more than 400 nozzles. This is one possible reason why high-performance CRF developed in the laboratory is difficult to reproduce in the industry. Nozzles affect each other during the production process, which leads to minor differences in the production conditions for each fiber. Because the proper viscosity and temperature required to produce CRF must be within a narrow range, small fluctuations may lead to a decrease in CRF quality. Unstable production causes more internal and external defects, which influence the mechanical properties. Another concern is the variation in the chemical and mineral compositions of rocks. Well-established companies typically rely on consistent rock sources from a single quarry location to maintain production stability. In contrast, laboratory experiments are designed to investigate various rock types, which complicates the process of sustaining the optimal production parameters for each distinct rock variety.

Basalt Screening and Characterization

The formation of basalt can be traced to its magmatic origin. The exsolution of volatiles from the melt leads to an eruption, during which a dramatic decrease occurs in the pressure and temperature of the melt. The ultimate chemical and mineral components of rocks depend on their thermal history, particularly their cooling rate, which affects the state change and chemical reaction procedure (Zhang, 2009). As the geographical and cooling conditions vary in the formation process, the components of basalt rocks in different places and mineral layers are different, which significantly affects the fiber production capability and performance. Table 1 shows the chemical composition of a basalt rock (Gutnikov et al., 2013), which can be measured using X-ray photoelectron spectroscopy (XPS), X-ray fluorescence (XRF) (Gutnikov et al., 2021), and energy-dispersive X-ray analysis (EDX) (Liu et al., 2023). FeO and Fe_2O_3 have been measured together in some studies to determine the exact partition between ferric and ferrous iron, which requires sophisticated analytical instrumentation or wet chemical methods (Ersoy et al., 2021). As shown in Figure 6a, the iron oxide content gives basaltic rock a dark color (from brown to dull green with the change in FeO content) (Mahltig & Kyosev, 2018). Basaltic rocks are generally fine-grained rocks, which make it difficult to classify using mineralogical methods. Instead, they are classified based on SiO_2, Na_2O, and K_2O weight percentages from the International Union of Geological Sciences (IUGS) or the total alkali–silica (TAS) diagram (Ersoy et al., 2021; Gutnikov et al., 2021). Figure 6b shows the TAS diagram for classifying the rock samples from different regions (Ersoy et al., 2021). The rocks used for CRF production include basalt, basalt andesite and andesites. Therefore, ''rock fiber'' is a more suitable term than ''basalt fiber'' for the description. The same research team later used the ternary phase diagram to classify the basalt rocks under Fe–Ti oxides (Fig. 6c) (Ersoy et al., 2022)

The weight percentage values of oxides do not reflect all attributes of the rocks, as the chemicals in the rock exist in the form of minerals instead of oxides. Optical microscopy and radiography are used to determine the mineral composition of igneous rocks (Krenev et al., 2022). As shown in Figure 6d I, thin sections of rocks can be used to analyze the type and size of the inner crystals through color differences, whereas scanning electron microscopy (SEM) in Figure 6d II combined with EDX allows for the distinction of different minerals such as clinopyroxene phenocrysts (1), chlorite (2), and actinolite (3) (Pisciotta et al., 2014). X-ray diffraction (XRD) is commonly used in research to check minerals in rock powder with a typical spectrum (Fig. 6e) (Dou et al., 2023). Approximately 80% of basalt consists of plagioclase and pyroxene (Militký et al., 2002; Fiore et al., 2015). However, the XRD result is semi-quantified, which only reflects a small amount of rock, making it difficult to accu-

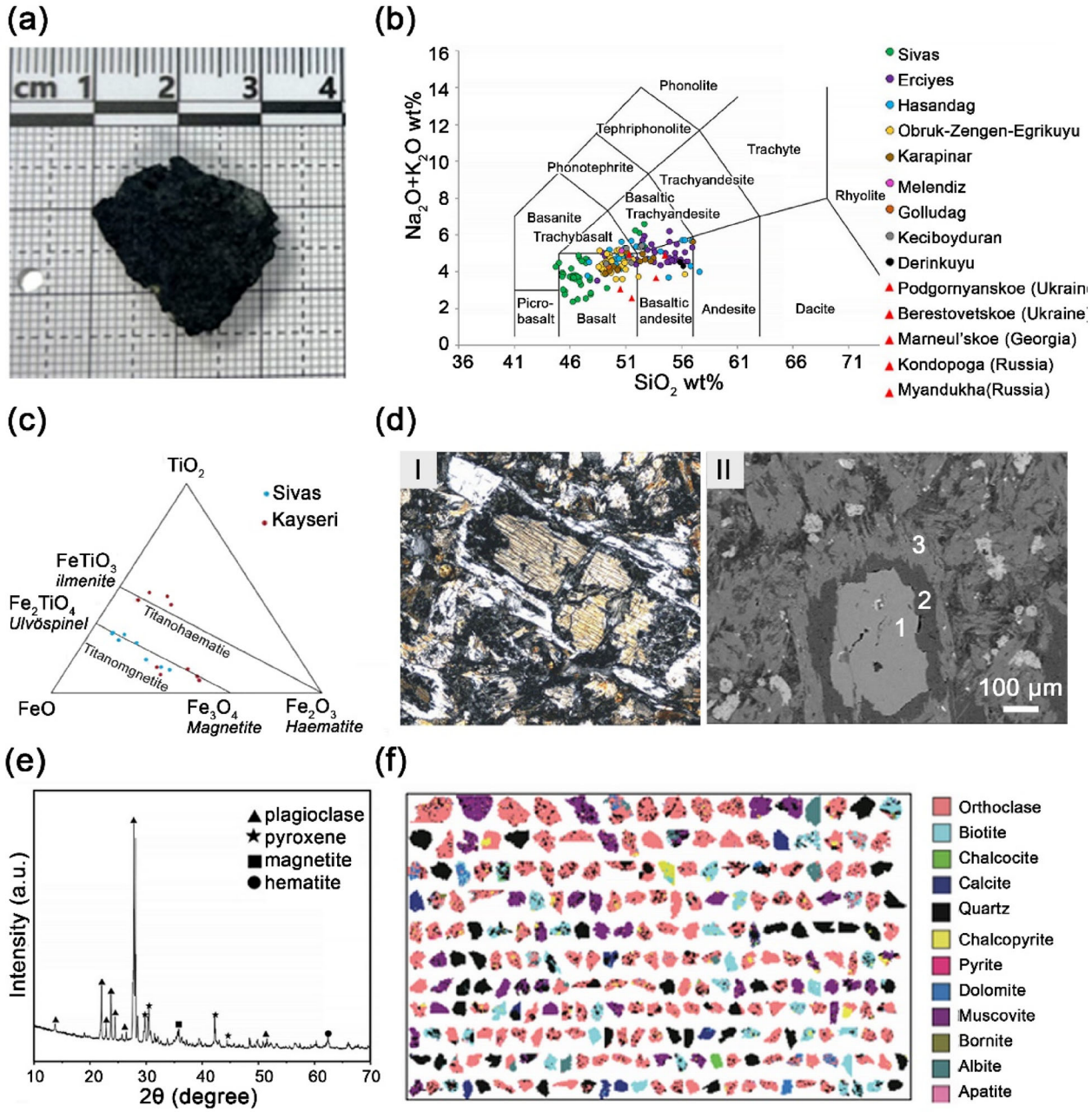

Figure 6. (**a**) A typical piece of basalt rock. (**b**) Total alkali–silica (TAS) classification diagram of Central Anatolia samples and reference samples (Ersoy et al., 2021). (**c**) TiO_2–FeO–Fe_2O_3 ternary diagram for Fe–Ti oxides (Ersoy et al., 2022). (**d**) (I) Porphyry allocation clinopyroxene with high relief and bright interference colors, partially substituted by chlorite (dark gray–gray scales with a brown tint) and white actinolite. (II) Electron microscopic images of basalt: clinopyroxene phenocrysts (1) surrounded by rims of chlorite (2) and actinolite (3) (Pisciotta et al., 2014). (**e**) XRD pattern of basalt rock (Dou et al., 2023). (**f**) Colored MLA-derived image sorted by particle area (Zhang et al., 2021).

rately analyze the effect of different minerals. Zhang et al. (2021) used a statistical method—quantitative mineral liberation analysis (MLA)—and XRD to characterize copper sulfide tailings (Fig. 6f). The method covered 12 different minerals and demonstrated the possibility of quantifying the mineral composition of basalt rock. CIPW (named for its inventors—Cross, Iddings, Pirsson, and Washington,

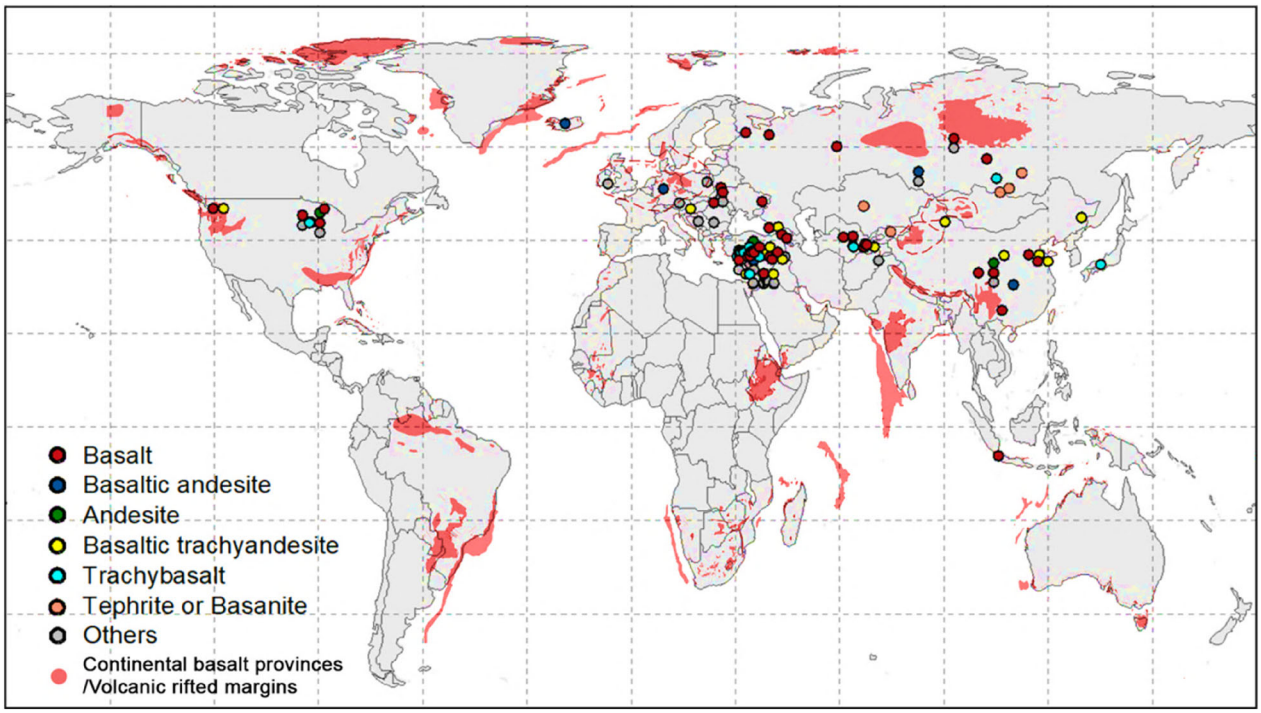

Figure 7. Overview of basalt rock sources mentioned in the literature.

(Cross et al., 1902)) is a method used in some studies to calculate the likely mineral compositions from the corresponding chemical composition (Morse, 1980; Chen et al. 2017a; Chen et al. 2020). However, the minerals calculated from CIPW cannot represent the actual minerals in basalt rocks. The accurate quantification of minerals in basaltic rocks is currently not feasible. Statistical results can satisfy the general production requirements, while hindering the study of the microstructure of rocks from a material science approach where accuracy in measurement is needed.

Limiting the scope of the Earth's crust (Iwamori & Nakamura, 2015), an overview of basalt rocks studied for RF production (Makhova, 1968; Dzhigiris et al., 1983; Militký et al., 2002; Tatarintseva & Khodakova, 2010; Wei and Song et al., 2011; Gutnikov et al., 2013; Novitskii & Efremov, 2013; Jamshaid & Mishra, 2016; Johannesson et al., 2019; Khudyakova et al., 2020; Chen et al., 2020; Wu et al., 2020; Meng et al., 2021; Ersoy et al., 2021; Liu et al., 2023) is summarized in Figure 7. Notably, the results were based on the sites mentioned in the research articles, which did not necessarily represent the source abundance or completeness of the data. Figure 7 depicts the sites of potential resources that could be adapted for CRF production through minimal alterations, such as the inclusion of additives or a reduction in thermal intensity. According to the claims, rocks from Ukraine (Makhova et al., 1984), Russia (Morozov et al., 2001), China (Chen & Huang, 2016), Iceland (Johannesson et al., 2019), Turkey (Ersoy et al., 2021), and other countries, such as the Republic of Buryatia (Khudyakova et al., 2020), were studied. Rocks from Ukraine are considered suitable for producing high-performance CRF (Jamshaid & Mishra, 2016). Owing to the transportation cost of the raw material, researchers are seeking possibilities to produce fibers with other rocks, such as gabbro (Krenev et al., 2022). Comparing the basalt storage in the red area of Figure 7, according to Self et al. (2014), with the currently reported rocks, it can be seen that there are several undiscovered sources with potential for exploration.

The empirical criteria for screening suitable basalt sources are mainly limited to the chemical components (Myasnikov & Aslanova, 1965). The SiO_2 content was considered the prioritized criterion. Rocks containing more than 50% SiO_2 are most likely to satisfy the other constraints (Johan-

Table 2. Criteria mentioned in the research

Parameter	Definition	Criteria (%)	References
SiO_2	Percentage by mass of SiO_2 in basalt rock	43– 60	Deák & Czigány, 2009)
Al_2O_3	Percentage by mass of Al_2O_3 in basalt rock	12–19	Johannesson et al. (2019)
FeO + Fe_2O_3	Percentage by mass of FeO and Fe_2O_3 in basalt rock	5–15	Johannesson et al. (2019)
Fe^{2+}/Fe^{3+}	Percentage by mass in basalt rock, iron redox amount	≥ 0.5	Chen, et al. (2017a)
CaO	Percentage by mass of CaO in basalt rock	6–12	Johannesson et al. (2019)
MgO	Percentage by mass of MgO in basalt rock	3–7	Johannesson et al. (2019)
TiO_2	Percentage by mass of TiO_2 in basalt rock	0.1–2	Johannesson et al. (2019)
Na_2O + K_2O	Percentage by mass of Na_2O and K_2O in basalt rock	0.5–5	Gutnikov et al. (2021)
M_a	Acidity modulus	3–8.5	Johannesson et al. (2019)
	$M_a = \frac{SiO_2+Al_2O_3}{CaO+MgO}$		
K_{total}	Acidity coefficients	1.7–2.35	Vasil'eva et al. (2014)
	$K_{total} = \frac{SiO_2+TiO_2+Al_2O_3}{CaO+MgO+FeO+Fe_2O_3+K_2O+Na_2O}$		
M_{total}	$M_{total} = \frac{\sum I_R^{2+}+0.5\sum I_R^{+}+1.5\sum I_R^{3+}+2\sum I_R^{4+}}{\left(I_{Al}^{3+}+I_{Si}^{4+}+I_{Ti}^{4+}\right)}$	2.3–2.6	Ersoy et al. (2021)
M_v	Viscosity modulus	2–3	Johannesson et al. (2019)
	$M_v = \frac{x_{SiO_2}+x_{Al_2O_3}}{2x_{Fe_2O_3}+x_{FeO}+x_{CaO}+x_{MgO}+x_{K_2O}+x_{Na_2O}}$		
NBO/T	A ratio of non-bridging oxygens per tetrahedron-coordinated cations	0–4	I. Gutnikov et al. (2019)
	$\frac{NBO}{T} = \frac{2\{[xNa_2O]+[xK_2O]+[xCaO]+[xMgO]+[xMnO]-[xFeO]-[xAl_2O_3]-[xFe_2O_3]\}}{[xSiO_2]+2[xAl_2O_3]+2[xFe_2O_3]+[xFeO]+[xTiO_2]+[xP_2O_5]}$		
M_{py}	Crystallization properties	2.75–2.85	Vasil'eva et al. (2014)
	$M_{py} = 2+\frac{\sum I_R^{2+}}{\sum I_R^{4+}-2\sum I_R^{1+}}$		
DI	DI = normative (quartz + orthoclase + albite + nepheline + leucite + kalsilite)	35–50	Ersoy et al. (2022)

R represents alkaline cations (Na^+, K^+, Ca^{2+}, Mg^{2+}), I_R^{n+} is the number of ions of mono-, bi-, tri-, and tetravalent elements in the basalt melt, and x is the molar percentage of the component in the rock.

nesson et al., 2019). The criteria are summarized in Table 2. One study promoted the differentiation index (DI), which has been used to quantify the degree of evolution that magma has undergone (Ersoy et al., 2022). DI can be used to screen rocks suitable for fiber production and to determine the type of fiber that the rock is suitable for, such as CRF or SRF. Other criteria include industrial production feasibility, such as accessibility and volume issues (Johannesson et al., 2019).

Basalt Melt

The melting process affects predefined CRF production parameters and the resultant fiber performance (Chen et al., 2017a). As a ''multi-component heterogeneous system'' (Krenev et al., 2022), the melting of basalt is a procedure with the low-melting minerals melting first, and the high-melting ones dissolve in the melt. The dissolution rate is affected by the heat-treatment time, viscosity, and surface tension of the melt (Pavlyukevich et al., 2023). On this basis, adjusting the melt temperature, such as the addition of CaO, was applied by Shi et al. (2024) in a SiO_2–Al_2O_3–Fe_3O_4–5 wt.% CaO system. They observed a single liquid region and three two-phase regions, including liquid-cristobalite, liquid-mullite solid solution, and liquid-spinel solid solution. When the low-melting minerals molten into the liquid phase, CaO dissolved into the liquid, expanding the liquid region, modifying the interaction among oxides, and may influence the surface tension and viscosity of the liquid phase. This change would alter the phase equilibrium relation and adjust the melting properties of the basalt rock.

The two parameters describing the basalt melt include the initial melting temperature T_{mi} and the final melting temperature T_{mf}. Novitskii & Efremov (2013) defined the two temperatures as: ''T_{mi} is the temperature of the primary rock melt and the sticking of the melt to the metal plate surface. T_{mf} is the temperature of complete spreading of the melted rock with a shiny, smooth melt surface, and must not

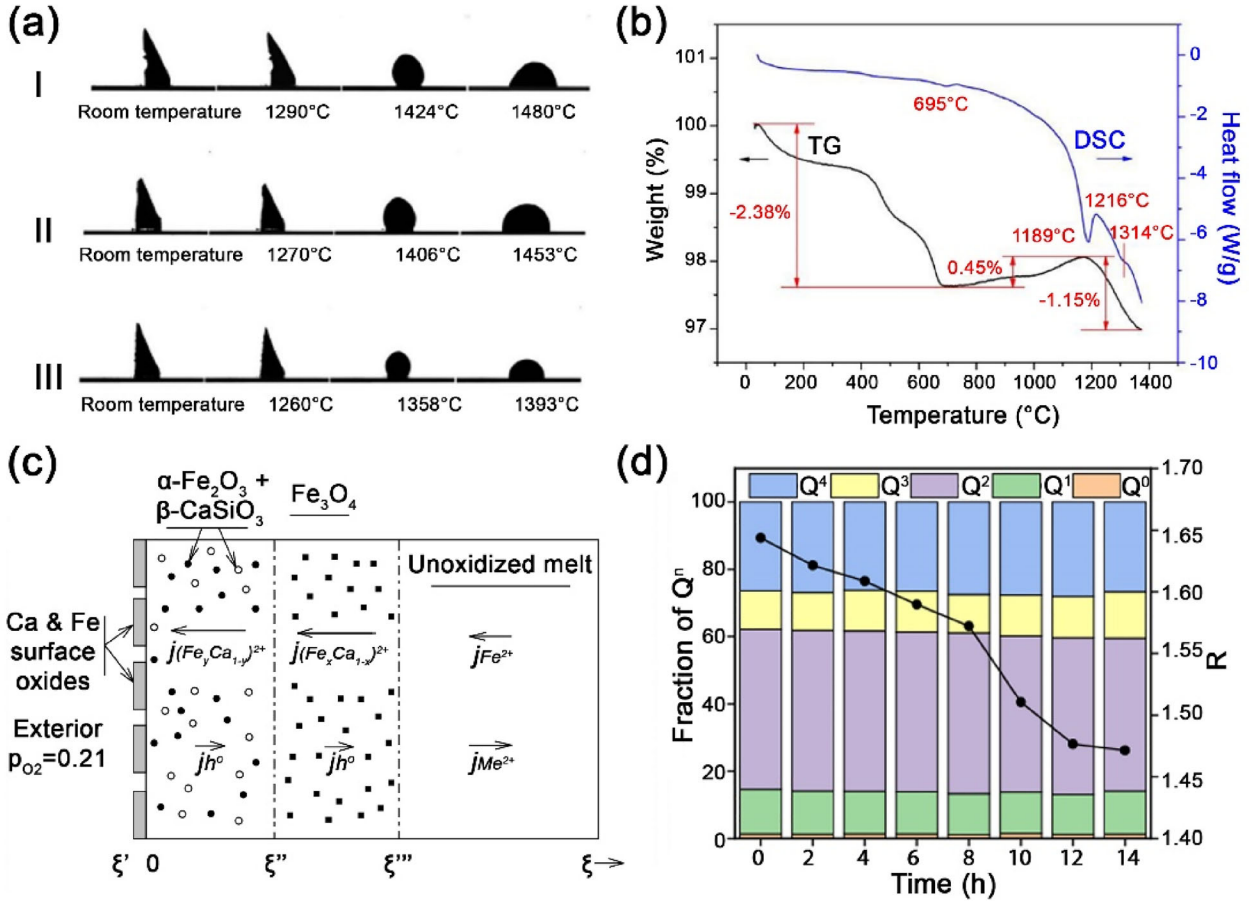

Figure 8. (**a**) High-temperature microscopic images and characteristic temperatures of basalts (I) AN; (II) ANB; (III) TB (Chen et al., 2017b). (**b**) TGA–DSC curve of basalt rock (Xing, 2020). (**c**) Schematic diagram of oxidation dynamics in molten basalt at 1400 °C (Cooper et al., 1996). (**d**) Fraction of structural units Q^n and R based on FT–IR spectra of basalt melts with different homogenization times (Dou et al., 2024).

have any visible crystalline and gaseous inclusions.'' These two temperatures can be measured under high-temperature microscopes (Fig. 8a) (Chen et al., 2017a), using rock samples, such as andesite (AN), andesitic basalt (ANB), and tholeiitic basalt (TB). The triangular pyramid became round, indicating the appearance of a liquid phase. When the sample transformed into a spherical shape and then collapsed downwards to form a hemisphere, the rock became completely molten. The recorded temperature readings were approximately 1110 °C and 1400 °C for T_{mi} and T_{mf}, respectively. After the complete melting, the heating temperature can be increased to the upper limit T_w, which is determined by the wettability of the equipment. The melt is then maintained between T_{mf} and T_w for a homogenization period in preparation for fiber drawing.

The heated rock undergoes evaporation, decomposition, redox reactions, melting, and crystallization. Differential scanning calorimetry (DSC) and thermogravimetric analysis (TGA) suggest that rocks from different sources (Chen et al., 2017a) undergo a similar process, with a moderate difference in the specific temperatures of the endothermic and exothermic peaks. Figure 8b (Xing, 2020) shows a typical TGA–DSC curve of a rock sample from Guizhou, China. The first endothermic peak of DSC at approximately 695 °C is associated with salt hydrate minerals and carbonate decomposition. Chen, et al. (2017a) noted a transfer from α quartz to β semiconductor-type transition at 575 °C. The second endothermic peak at approximately 1189 °C is associated with plagioclase and diopside melting and orthoclase decomposition. The third endothermic peak at 1314 °C indicates the melting of other min-

erals into a liquid. A prominent exothermic peak occurs at 1216 °C, which indicates the highest crystallization temperature T_c of the melt. The rocks are completely molten after approximately 1314 °C. The corresponding TGA curve shows weight loss until 700 °C due to water evaporation and mineral decomposition, a weight gain at approximately 700–1170 °C due to the oxidation of magnetite, and a weight loss at 1170–1420 °C with mineral decomposition.

The process highlights a parameter $T_{c.}$ different from T_{mi} or T_{mf}, as the microstructure of the crystals undergoes a lattice opening process (Wu et al., 2020), during which the ordered structures are destroyed and form a three-dimensional disordered state. The structure is semi-stable and prone to crystallization under T_c. Notably, the temperature described is usually a range reflected from a broad exothermic peak in DSC with the crystallization temperature of plagioclase (1087–1100 °C), pyroxene (889–973 °C) and spinel (593–642 °C), affected by the methods of quenching (Krenev et al. 2020; Si et al., 2021). Because a fast-cooling process is used to form basalt glass, it is crucial to draw fibers at temperatures above the highest T_c to restrict the formation of crystal cores. Crystal cores lead to fast crystallization, breakage of the fiber, and a decrease in CRF tensile strength. T_w and T_c are the upper and lower boundary ranges of the fiber drawing temperature (Bauer et al., 2018).

A critical change in the melting process is the oxidation of iron, which affects all steps from basalt melting to glass formation and crystallization. Cooper et al. (1996) mentioned the diffusion of Fe^{2+} and Ca^{2+} to the melt surface, whereas the internal oxidation of the melt resulted from the required counter flux of electron holes (Fig. 8c). Magnetite was formed as the crystal core. Notably, the crystallization process that occurred in the melt also occurred during the CRF crystallization stage under heat treatment (Xing et al., 2022) (Fig. 12 g). Magnien et al. (2008) studied the iron redox reaction in basalt melt using Raman spectroscopy and X-ray absorption near edge structure (XANES). They proposed that the diffusion of divalent cations is the dominant iron redox mechanism at low temperatures, whereas the diffusion of oxygen is the major mechanism at super liquid temperatures. A limited number of studies were found in analyzing the kinetics in the melt process.

After the rock is molten, viscosity η can be measured using a high-temperature rotational viscosimeter, concentric cylinder viscometer, or micropenetration viscometer (Yue & Zheng, 2017). From an energy standpoint, η represents the amount of energy required for the molecules in the molten state to overcome the potential energy barrier and move freely. This parameter reflects the energy requirements for molecular mobility within the liquid melt. This energy is defined as the viscosity activation energy E_0. The relationship between η and E_0 can be expressed using the Arrhenius equation (Arrhenius, 1889), thus:

$$\beta = A\exp\left(\frac{E_0}{kT}\right) \tag{1}$$

where A is a constant, k is Boltzmann's constant, and T is the temperature. Martinez & Angell (2001) suggested that for silica glass, E_0 can be regarded as constant when the temperature is not close to the glass transaction temperature T_g, thus the formula can be expressed as:

$$\lg\lg\eta = A_0 - B_0\lg T \tag{2}$$

After measuring a series of η and the corresponding temperature, Eq. 2 can be fitted into a linear function with A_0 and B_0 being two constants. Another well-known three-parameter model describing the supercooled liquid viscosity near T_g is the VFT formula (Vogel, 1921; Fulcher, 1925):

$$\log\eta(T) = A_{VFT} + \frac{B_{VFT}}{(T - T_0)} \tag{3}$$

where T_0, A_{VFT} and B_{VFT} are obtained by fitting experimentally measured viscosity data. The model has been used to fit the soda–silica glasses, but the physical meaning of the formula requires further explanation.

The homogenization of the melt is important to ensure that the glass forms a uniform microstructure. Owing to the dark color of the iron content, the heat radiation from the heating units is inconsistent in the melt from the surface to the bottom of the furnace. Dou et al. (2024) studied the homogenization temperature and time based on Gaussian fitting of the Fourier transform infrared spectroscopy (FT–IR) spectra (Fig. 8d). The R-values equal to $(Q^0 + Q^1 + Q^2)/(Q^3 + Q^4)$ of basalt melts decreased with increasing homogenization time, indicating that the increase in temperature leads to a decrease in the degree of polymerization for basalt melts above 1400 °C. Moreover, a lower η indicates a less com-

pact microstructure, but leads to better homogenization.

In general, the parameters in the melting stage are T_{mi}, T_{mf}, T_w, T_c, η and degree of homogenization. T_{mi}, T_{mf}, T_w, and T_c reflect the properties of the crystals in the rock before complete melting. T_w and T_c set the upper and lower limits of the melt temperature. While researchers have clarified the melting process of various rocks, the relationship between the microstructure and T_c, and the oxidation kinetics of iron during melting are worth further exploration. Moreover, while the mentioned temperatures are easily measured in labs with small rock samples, they are difficult to obtain in industrial furnaces as the initial melting stage is not homogenized with local variations in crystal content and uneven heat transfer. The viscosity and degree of homogenization reflect the melt property. The η–T relationship was analyzed using the theoretical model, which reflects the internal microstructure of the melt. There is by far no single parameter to quantify the degree of homogenization. It is generally assumed that the melt is homogenized after a period that is sufficiently long; however, this assumption might lead to contradicting experimental results. With the development of some patents (Cao et al., 2019), continuous monitoring of viscosity at high temperatures remains costly and challenging in the CRF industry.

Cooling and Fiber-Drawing Process

When the melt is quenched, the microstructure of the melt is ''frozen'' and forms the basalt glass. The transformation from basalt melt to glass is based on the schematic time–temperature–transformation (TTT) diagram proposed by Uhlmann (1972) in Figure 9a. The range of T_g can be measured under the DSC when heating the basalt glass, with the first endothermic peak shown in Figure 9b (Liu et al., 2020a). From an empirical relationship (Zallen, 1983), T_g can be estimated to be:

$$T_g \approx \frac{2T_m}{3} \tag{4}$$

where T_m is the melting temperature of the single crystal substance. In Figure 9a, the cooling rate is an underlying parameter, apart from T_m and T_g, which affects the polymerization degree of the glass. The drawing temperature, or manufacturing temperature T_d is a range (T_{dl} – T_{dh}) between the T_w and T_c under which the CRF can be drawn stably. Fiber production is considered to be stable when there is almost no breakage or melt pulsation at the nozzle and the fiber diameter is uniform.

Assuming that the melt flows like a continuous Newtonian fluid and takes the direction of gravity in the positive direction, the numerical analysis was conducted based on balances in mass, force, momentum, and energy. From the mass balance, the molten basalt flux through nozzle Q is calculated using Poiseuille's law (Sutera & Skalak, 1993), thus:

$$Q = \frac{\Delta P \pi R_0^4}{8\eta l} \tag{5}$$

where R_0 is the nozzle diameter, l is the nozzle length, and ΔP is the pressure loss which is regarded as a constant with a stable melt height in the furnace. Consider this amount of melt was taken to draw fiber with a density of ρ, the radius of r_0 under drawing speed v_d was calculated by Kim et al. (2013) as:

$$r_0 = R_0 \sqrt{\frac{k\sigma_0}{\rho v_d}} \tag{6}$$

where k is a constant, and σ_0 is the yield stress of the molten basalt flow in the nozzle. Equation 6 reflects the negative relationship between yarn diameter and drawing speed. This relationship was verified in experiments by Gutnikov & Lazoryak (2019) using nozzle diameters of 1.5, 2.5, 3.5, and 4.5 mm and drawing speeds from 300 to 1200 m/min. The result showed that, with increase in nozzle diameter from 1.5 to 4.5 mm, the fiber diameter increased by 6.5–9 times, whereas an increase in winding speed led to a decrease in fiber diameter (Fig. 9c I).

Yan & Yan (2004) and Gutnikov & Lazoryak (2019) analyzed the drawing process (Fig. 9c). In a stable drawing process, the melt undergoes a force balance between the negative direction, that is, the surface tension F_σ, the viscous force F_η, the friction between the melt and air F_f, and the positive direction; that is, the winding (drawing) force F_w and the gravity of the melt G_m, thus:

$$F_\sigma + F_\eta + F_f = F_w + G_m \tag{7}$$

Kim et al. (2013) provided a detailed diagram (Fig. 9c). The melt to fiber process was divided into three parts: the upper flow with a length of z on the gravity direction, a middle flow with a length of

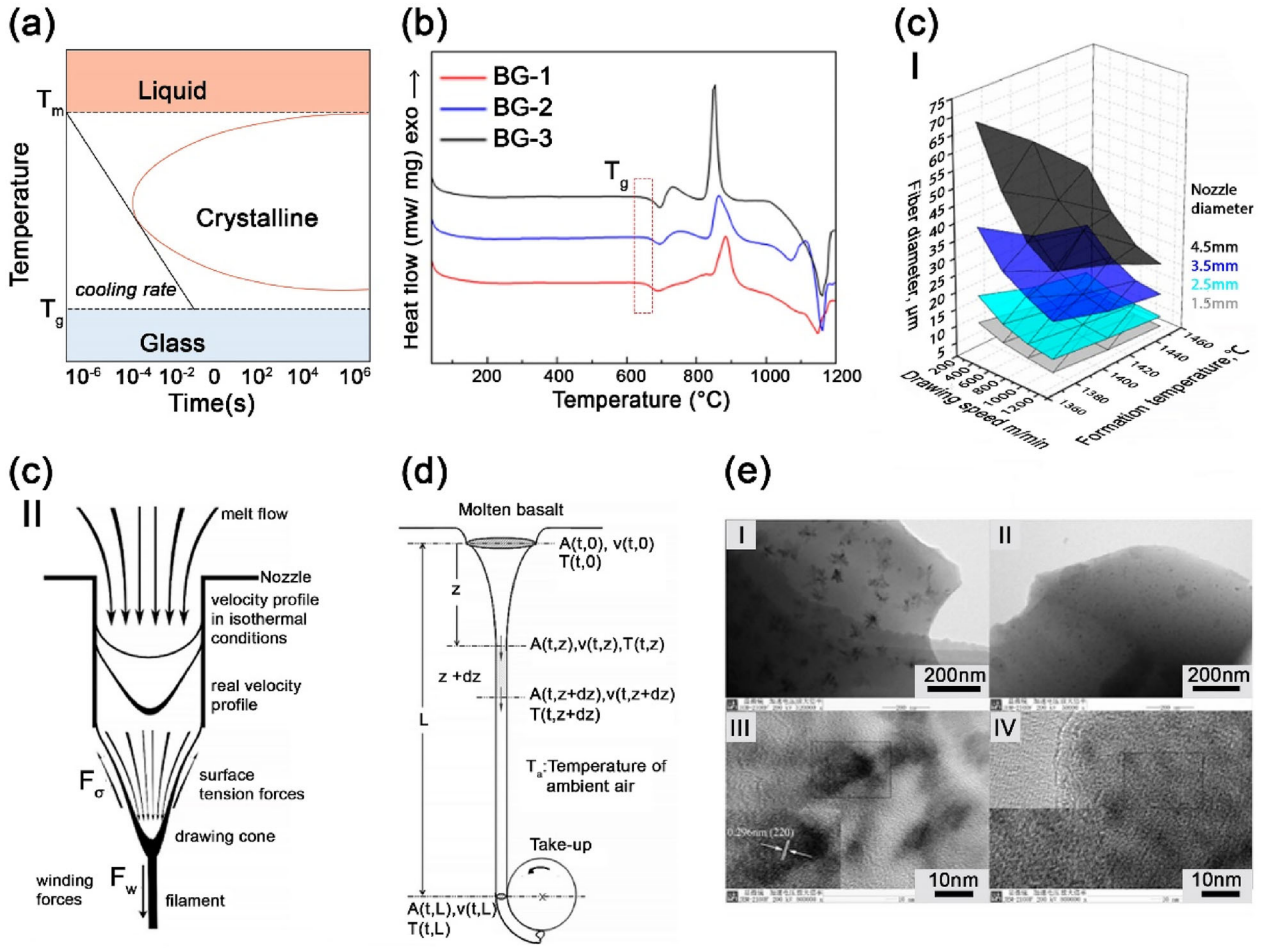

Figure 9. (**a**) Time–temperature–transformation diagram. (**b**) DSC analysis of basalt glasses (Liu et al., 2020a). (**c**) (I) Dependence of diameter of the CRF on winding speed and formation temperature. (II) Schematic diagram of the distribution of flow velocity in the basalt melt through the nozzle and in the drawing cone (Gutnikov & Lazoryak, 2019). (**d**) Schematic diagram of the RF spinning process (Kim et al., 2013). (**e**) TEM photographs of the melt (sample BG) prepared from raw basalt (I, III), and from mixtures (II IV) with added 3.0 wt% CaO (Si et al., 2021).

z + dz, where the melt was cooled rapidly, forming the cylindrical fiber shape, and the lower part with solidified basalt fiber being drawn onto the winding machine, with the drawing height of L. Yan & Yan (2004) suggested that F_σ can be calculated as:

$$F_\sigma = 2\pi\sigma r_0 \cos\theta \tag{8}$$

where σ is the surface tension coefficient, r_0 is the radius of the melt cross section, and θ is the angle between the free surface of the melt and the z-axis. The F_η can be calculated as:

$$F_\eta = -\frac{6\eta Q_m}{\eta_f r_0}\frac{dr_0}{dz} \tag{9}$$

where Q_m is the mass flow of the melt in kg/s. Equations 8 and 9 show that the parameters of the melt are of great importance in maintaining a stable drawing process. Therefore, T_d is defined based on the proper η value that maintains this balance. Yue & Zheng (2017) used a concentric cylinder viscometer and a micro-penetration viscometer to measure the viscosity of the melt. Their findings indicated that for continuous fiber drawing, η should range from 50 to 200 Pa. The upper and lower limits of the viscosity form a ''viscosity window,'' corresponding to T_{dl} and T_{dh}. Johannesson et al. (2019) suggested a narrower viscosity window of 10–30 Pa in the T_d range 1380–1440 °C. The current numerical model simplified the phase change from melting liquid into glass, especially in the

middle flow. A model combining the glass transition effect is expected to be more accurate and provide a more insightful relationship.

When the production parameter can be controlled and designed, the variables that remain are η and the corresponding T_m, T_c, and T_g, which are affected by the chemical and mineral components. SiO_2 as the NF maintains a positive effect on the formation of the glass network, resulting in a high T_m and η. Novitskii & Efremov (2013) suggested that rocks with a SiO_2 content of more than 50% tend to have a higher T_{mf}. The percentage of SiO_2 was found to ensure that the rock melted without residues (Mahltig & Kyosev, 2018). However, SiO_2 with over 57wt% was found to cause too high a viscosity to form CRF. Mg^{2+}, Ca^{2+}, Na^+, and K^+ are NM, causing a decrease in T_m (Chen, et al., 2017b). Gutnikov et al. (2009) verified that the aluminum lowered the T_{dh}, probably because of an increase in η. Kuzmin et al. (2016) proved the addition of alkali oxides reduced the η, thus leading to decrease in T_{dl}. The effect of the chemical composition leads to an expansion or shift in the viscosity window and the resultant T_{dh} and T_{dl} values.

As empirical models with chemical composition and viscosity, the early model of Bottinga & Weill (1972) assumed that the viscosity of a silicate melt can be expressed as an additive function of the molar fractions of their oxide components X_i, with SiO_2 concentration 0.35 to 0.81, which covers the SiO_2 range of basalt rock, thus:

$$\eta = \sum_{i=1}^{i} X_i D_i \tag{10}$$

where D_i is a regression coefficient obtained by fitting viscosity melt data from a variety of chemically simple systems. The model was based on 2440 datapoints from the literature under a temperature range of 1200–1800 °C, showing satisfactory agreement with the published magma viscosities. Makhova et al. (1990) used computer programs of multifactor regression analysis to study the relationship between chemical composition and the melt viscosity under 1300–1400 °C. The individual contributions of nine chemical compositions to viscosity were reflected in the model. The study revealed that the viscosity exhibited positive correlations with the molar amounts of SiO_2 and Al_2O_3. Inverse correlations were observed between viscosity and compounds including Fe_xO_y, MgO, CaO, Na_2O, K_2O, and TiO_2. Rock type variations influenced the correlation coefficients, pointing to a collective impact on viscosity. When the temperature changed from 1400 to 1300 °C, the effects of SiO_2 and Al_2O_3 on viscosity were suggested to be lowered. The empirical relationship was optimized by Tatarintseva et al. (2012), including the acidity modulus M_a, which was concluded to be:

$$\eta = 3.62(SiO_2)^{3.07}(Al_2O_3)^{-0.16}(CaO)^{-0.4}(FeO + Fe_2O_3)^{1.34}(M_a)^{1.25}(T-1100)^{-2.58} \tag{11}$$

This formula was used by Ersoy et al. (2021) to evaluate the suitability of rocks in Turkey for CRF production.

The effect of the mineral composition on η follows a continuous random network model. A more compact structure, such as that found in phyllosilicates, results in a higher η. According to Chen et al. (2017a), the presence of olivine as an infusible mineral in the melting of basalt should be considered as a reason to exclude it from manufacturing processes. Liu et al. (2023) prepared the artificial stimulant with the same chemical composition as natural basalt and concluded that the materials with the same chemical composition perform similarly in thermal behavior but differ in their minimum and maximum drawing temperatures. The detailed effect of mineral components on viscosity and the extent to which the mineral structures are destroyed to form the glass structure require experimental verification. Unavoidably, crystallization occurs along the CRF-forming stages, which has a direct effect on CRF quality. Novitskii & Efremov (2013) reported that andesitic porphyrite has a relatively low upper limit of T_c. Militký et al. (2002) suggested that the abundant amount of iron oxides (10–15%) and the low alkali of the basalt would increase the T_c. They reported crystallization temperatures for magnetite (720 °C), pyroxene (830 °C), and plagioclase (1010 °C). Si et al. (2021) reported that CaO reduces the degree of CRF polymerization and increases the amount of nonbridging oxygen. Figure 8f shows a reduced number of crystals under transmission electron microscopy (TEM) with CaO addition of 3 wt%, which inhibited the crystallization of spinel and promoted the crystallization of pyroxene and plagioclase.

In the cooling and fiber drawing stages, numerical models have been established with certain simplifications, while the microstructure change of the glass transition process under fast cooling remains unclear. To date, the fluid–structure interac-

tion within material has not been investigated. Some intuitive relationships can be drawn but require further experimental validation. As a crucial property, the viscosity has been predicted with empirical models based on the chemical composition, while the study of the change of microstructure from mineral crystals to the melt and the short-, middle-, and long-range order of the formation of glass needs further explanation. Moreover, CRF is generally considered to be isotropic, similar to basalt glass; if the drawing and cooling processes affect the rearrangement of the microstructure, the structural difference between the fiber core and surface, and the effect of the asymmetrical radial temperature field is one aspect worth studying.

Elastic Modulus

The elastic modulus of CRF is typically defined as the slope of the stress–strain curve in the elastic deformation region when stretched along the fiber axis. Here, the elastic modulus is referred to as Young's modulus E, whereas the elastic constants include the shear modulus G, bulk modulus B, P-wave modulus, and Poisson's ratio γ_p. Because RF is considered isotropic, its elastic behavior is described using two of the nine elastic constants: E and γ_p. In early study on CRF (Andreevskaya & Plisko, 1963), the E of the cylindrical basalt fiber was obtained using the impulse ultrasonic method with a guided wave method (Schreiber et al., 1973). This result is closer to the transient modulus, which can be measured using nanoindentation (Liu et al., 2020a) or DMA. Currently, quasi-static measurements remain the mainstream testing method.

Considering microstructure, E is equal to the second derivative of the overall atomic binding energy, reflecting the bonding between the atoms. The MM model (Makishima & Mackenzie, 1973, 1975) calculates the E of crystals. As the Madelung constant is considered unsuitable for describing disordered glass materials, the MM model involves the packing density (Rouxel, 2006) and was introduced for polycomponent glass, thus:

$$E = 2V_t \sum_i G_i X_i \tag{12}$$

where Gi is the dissociation energy per unit volume of component i, X_i is the mole fraction of component i, and V_t is the packing density, where M is the effective molecular weight, and ρ is the density. Wu et al. (2020) suggested that the property of the mixed rock can be calculated from:

$$E = 2\frac{\rho}{\sum X_i M_i}\left(\sum X_i V_i \sum X_i G_i\right) \tag{13}$$

where M_i is the molar mass of component i. Xu et al. (2024) used the Gan Fuxi model to predict the GF with iron series.

The parameters affecting the elastic modulus are explained in two ways. The first is similar to η, using the continuous random network model with the role of the chemical components as NF, NM, and mediators. When analyzing the CRF end structure, more NF in the glass would contribute to a more compact glass network, leading to an increase in modulus. As reported by Deák & Czigány (2009) (Fig. 10a), the ceramic-like content (SiO_2 + Al_2O_3) shows a correlation coefficient of 0.8 with the elastic modulus. On the other hand, NM has the contrary effect, and the mediator plays a dual role. The CRF after deferrization (DCRFs) produced by Manylov et al. (2015) showed an improvement in elastic modulus compared to the original CRF (Fig. 10b). This is because a lowered content of NM iron cations and increased percentages of NF silicon and aluminum cations improved the modulus. However, an improvement in the elastic modulus of basalt glass was reported by Chen et al. (2022) using nanoindentation. As shown in Figure 10c, the elastic modulus of RF1 increased from 91 to 98 GPa with increase in 6 wt% Fe_2O_3.

Another explanation is based on the definition of the elastic modulus and microstructure including packing density, rotation of silicate tetrahedrons, and covalent bonds. Kuzmin et al. (2016) suggested that an increase in packing density led to impeded Si–O bond angle and distortion, which increased the elastic modulus. The degree of connectivity in the glass increased from a chain-like to a layered structure. The density, packing density, and elastic modulus were measured and calculated by Liu et al. (2020b). The result indicated that a high packing density led to a relatively high elastic modulus. Contrary to the initial explanation suggesting that NM reduces the modulus, Kuzmin et al. (2017) reported that CRF exhibited a 13% enhancement in elastic modulus after 15 wt% MgO addition. The elastic deformation of the glasses occurs through mutual rotations of the tetrahedrons (Fig. 10d). A greater cation charge from Mg^{2+} hinders the rotation

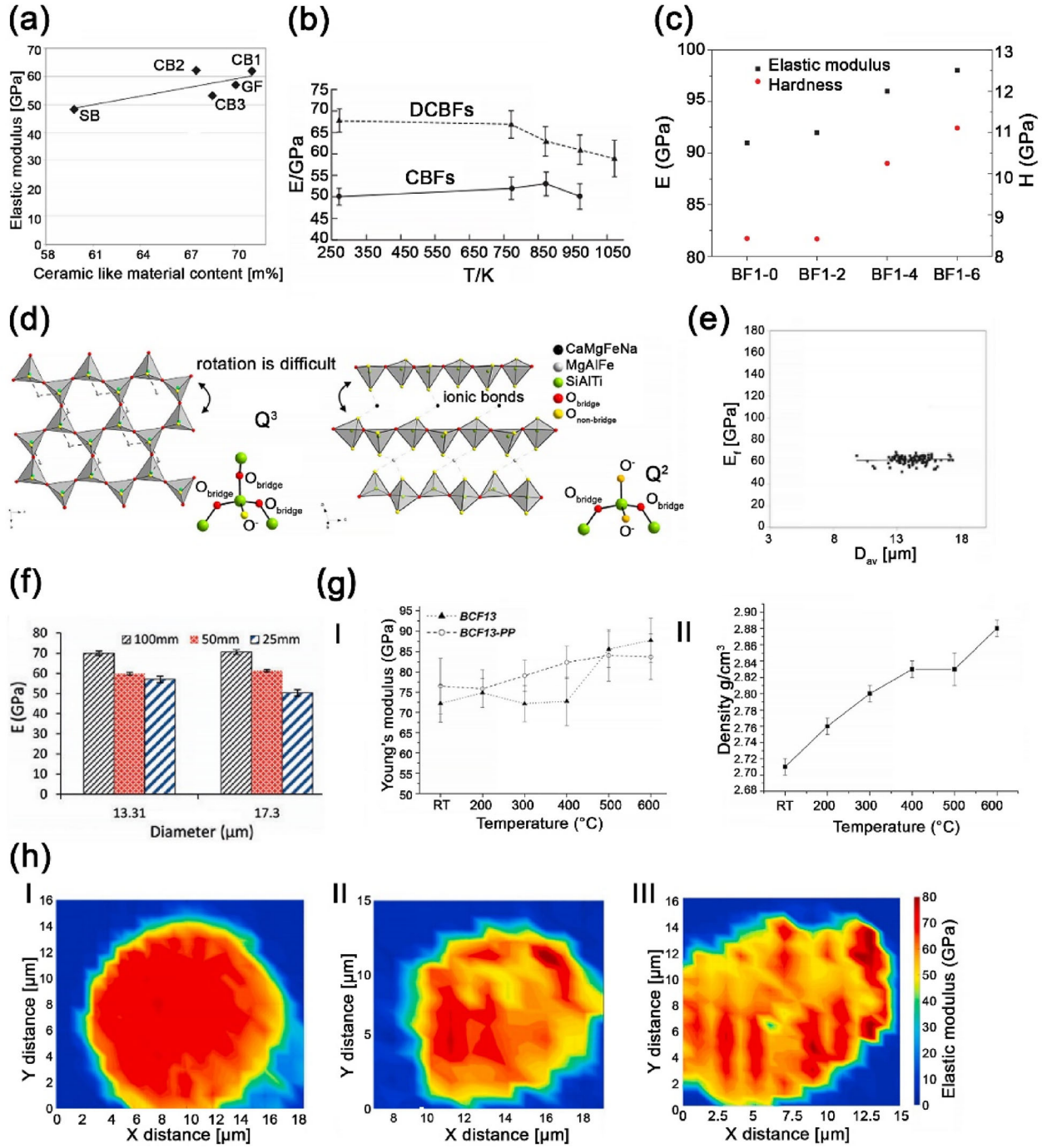

Figure 10. (**a**) (I) Correlation of ceramics (SiO_2 and Al_2O_3) content and elastic modulus of investigated fibers (Deák & Czigány, 2009). (**b**) Elastic modulus of CRFs and DCRFs before and after heat treatment for 1 h in air at different temperatures (Manylov et al., 2015). (**c**) Elastic modulus and hardness of basalt glasses with addition of 2, 4, and 6wt% of Fe_2O_3 (Chen et al., 2022). (**d**) Different aluminosilicates structural fragments with main chemical bonds (Gutnikov et al., 2021). (**e**) Diameter–elastic modulus relationship of CB1 (Deák & Czigány, 2009). (**f**) Diameter–tensile modulus relationship for sample RF5 (Ralph et al., 2019). (**g**) (I) Young's modulus as a function of temperature for BCF13 and BCF13-PP fibers treated in air. (II) Density of BCF13 fibers as a function of heat-treating temperature in air (Sarasini et al., 2018). (**h**) An elastic modulus map as obtained by high-speed nanoindentation method for basalt fiber in the (I) untreated condition (II) after thermal treatment at 450 °C for 1 h, and (III) after thermal treatment at 600 °C for 1 h. (Lilli and Rossi et al., 2020).

and displacement of the charged tetrahedrons, thereby increasing the elastic modulus. Gutnikov et al. (2019, 2021) measured the mineral composition of 14 basalt rocks, which suggested a positive correlation between elastic modulus and tectosilicate minerals (wt%) with a Pearson correlation coefficient (PCC) of 0.7 and a negative correlation between chain and layered aluminosilicates (PCC-0.74). They concluded that the stronger the covalent bonds, the more difficult it is to change the position of the silicon–oxygen tetrahedrons, and thus, the higher the elastic modulus.

In glass forming and fiber drawing, defects and scratches can be observed on the fibers. Gur'ev et al. (2001) tested the modulus of CRF roving and air-blown basalt wool, suggesting that the volume defects and their distribution in the longitudinal and radial directions, or on the fiber surface, did not have a significant effect on the elastic modulus. Moreover, a negative dependence of the elastic modulus on the fiber diameter has been reported. However, Deák & Czigány (2009) concluded that the elastic modulus is independent of the diameter (Fig. 10e), which was further confirmed by Ralph et al. (2019) The difference might be caused by the testing procedure; Gur'ev et al. (2001) conducted their experiments with heat-treated fiber roving, whereas the latter two conducted the tests at room temperature. Sarasini et al. (2018) suggested no significant dependence of the elastic modulus on gauge length (GL), while Ralph et al. (2019) proposed that although the diameter had almost no effect, the fiber with longer GL showed an increase in the elastic modulus as shown in Figure 10f, but the effect was not obvious after removing the values for GL of 100 mm.

Regarding the elastic modulus of CRF under heat treatment, Černý et al. (2011) used a purchased fiber bundle to test the elastic modulus at different temperatures (580, 640, 840, and 700 °C) in a furnace, observing a 13% drop in modulus at 450 °C. Bhat et al. (2017) found no obvious change in the elastic modulus after heat treatment from 250 to 650 °C for 2 hours. Manylov et al. (2015) reported a slightly increased elastic modulus after heat treatment to 750 °C (Fig. 10b). This phenomenon was emphasized by Sarasini et al. (2018) in Figure 10g I . A structural arrangement may have occurred during thermal exposure, leading to an increase in the elastic modulus accompanied by a thermal compaction phenomenon with an increased density (Fig. 10g II). A comparable explanation involving heat treatment of CRF was put forward by Boutenel et al. (2020) and Xing et al. (2022), with temperatures reaching up to 1000 °C, and 350 °C for 10 hours followed by 600 °C for 35 minutes, respectively. Lilli et al. (2020a) used high-speed nanoindentation mapping to visualize the change of elastic modulus on the fiber cross section as shown in Figure 10h, I, II and III which confirmed the increase of the average elastic modulus after thermal exposure. The analysis revealed a slight variation in the modulus across the fiber's diameter, with values increasing from the inner core toward the outer skin. The anisotropy relaxation, in terms of local structural rearrangements and loss of axial orientation of defects, appeared to be non-homogeneous across the fiber diameter and mainly concentrated in the skin. However, Rouxel et al. (2007) reported a general decrease in the elastic modulus after heat treatment of an amorphous material. As the fiber material, heating temperature, and heating time were inconsistent in different studies, the reason for the increase in the elastic modulus after heat treatment and the corresponding change in the microstructure remains debatable.

Studies on the elastic modulus of basalt glass can provide insights from research on other glass materials. Yang et al. (2019) suggested that the elastic modulus of glass generally increases with increasing network connectivity. Studies on amorphous alloys revealed that the elastic modulus is primarily influenced by the yield stress and T_g, rather than the chemical composition (Galimzyanov et al., 2023), with a linear relationship expressed as: $T_g \propto 2.5E$ (Wang, 2005). Different from the crystalline materials, the elastic moduli of the SiO_2-based glasses are found to be determined by the atomic bonding strength, glass structural features, such as atomic packing density, cation coordination numbers and ring, chain, layer sizes (Hu et al., 2020). The additive oxides besides SiO_2 introduce cations with various valence states, which not only change the cation-oxygen bonding strengths but also modify the degree of network polymerization (Hu et al., 2020). The research mentioned above can be referred to when studying the composition and structure–elastic modulus relationship of CRF.

Current research on the elastic modulus of CRF remains limited, which is usually discussed as an affiliated parameter to tensile strength. However, the elastic modulus provides a more direct insight into the microstructure, as it is less affected by de-

fects and external factors than the tensile strength. There are many points worthy of further discussion summarized as follows. Regarding the diameter, theoretically, variations in diameter lead to a different cooling rate of the glass, which should impact the compactness of the glass network and, consequently, affect the elastic modulus. However, the experimental results did not support this expectation. Another aspect refers to CRF after heat treatment. Crystallization at 750 °C with a more compact microstructure should increase the elastic modulus, whereas a decrease was observed beyond 750 °C (Fig. 10c). In general, the correlation between the microstructure and the elastic modulus is not fully explained or characterized. The two explanations mentioned above regarding the role of NM have contradictory points on the connectivity and deformation of the network. The packing density, rotation of silicate tetrahedrons, and covalent bonds are worth verifying through MD and characterization based on the study of other amorphous materials such as silica glass and amorphous alloys.

Tensile Strength

Tensile strength is the most extensively studied mechanical property of CRF. It refers to the maximum stress that the fiber can withstand while being stretched before breaking, corresponding to the highest point of the stress–strain curve when stretching the fiber along the axis direction. The following must be considered when studying the tensile strength and associated parameters:

- Clarify the chemical composition of the rock, basalt glass, or CRF, as they can be different due to redox reactions in the production process.
- Sizing is usually applied to industrial CRF. However, sizing or surface treatment has not been mentioned in some experiments, which could bias the conclusion (Sokolinskaya et al., 1991).
- Testing procedures, such as drawing fiber out of a bundle or pinning fiber onto a card tab, were suggested to damage or influence the tested mechanical properties (Chen & Huang, 2016).

The tensile failure strength of brittle materials, such as glass or basaltic fibers, can be regarded as a function of the surface flaws present, following Griffith's theory (Griffith, 1921), which reflects one type of internal defect. It explains the breaking strength tested is usually smaller than the theoretical result. As brittle glass material, the tensile strength of the CRF can be estimated to be equal to its tensile strength without considering the elastic deformation. The GL effect of brittle fibers refers to a higher tensile strength at a shorter GL, as longer fibers have a greater possibility of having fatal cracks (Jung & Subramanian, 1993). Therefore, the mean tensile strength fails to provide a comprehensive representation of the sample characteristics. Statistical and probabilistic methods using two-parameter Weibull (Weibull, 1951) calculations have been used to compare the ultimate tensile strength (Militky & Kovacic, 1996; Militký et al., 2002; Chen & Huang, 2016). Assuming that fiber breakage is caused by a fatal defect in the fiber, the failure probability is when the tensile strength is not higher than F(σ_t), thus:

$$F(\sigma_t) = \frac{n}{N+1} \tag{14}$$

where n is the number of single fiber failures at the tensile strength, and N is the total number of samples. The relationship between $F(\sigma_t)$ and GL can be expressed as:

$$F(\sigma_t) = 1 - \exp(-GL(\frac{\sigma_t}{\sigma_{t0}})^m) \tag{15}$$

where m, σ_{t0}, and σ_t are the shape parameter, scale parameter, and actual tensile strength, respectively. A larger value of m reflects a more even distribution of the defects; m and σ_0 can be obtained by fitting $\ln\ln(1/(1-F(\sigma_t)))$ and $\ln\sigma_t$ plots based on:

$$\ln\ln(1/(1-F(\sigma_t))) = m\ln\sigma_t + \ln GL - m\ln\sigma_{t0} \tag{16}$$

Conversely, the Maxwell model (Lamb, 1978) was used by Shebanov et al. (2022) to explain the viscoelastic properties of RF, glass, and aramid fibers over time. The viscoelastic property may reflect another type of defect in the form of a flow unit (Wang, 2023). Other models, such as a statistics-based optimization model specifically focused on CRF, were established using the LINGO software by Meng et al. (2021) using M_a and M_v, which was verified by one experiment of mixing two rocks. The boundary condition used was to maximize the tensile strength, which is another possible modeling approach.

The role of the chemical component refers to the continuous random network model, with silica tetrahedra as the major NF. It is generally believed that a tighter network structure connection results in higher tensile strength (Liu et al., 2018). On the other hand, as the defects and flaws would affect the tensile strength, a homogenized structure with less ''flaws'' shows a higher tensile strength statistically. Chen et al. (2020) concluded that SiO_2 was the main parameter affecting the tensile strength after comparing ten basalt samples. Chen et al. (2017a) produced CRF with a mixture of basalt rocks in different amounts of SiO_2. The bare CRF drawn from mixtures with higher SiO_2 contents exhibited higher tensile strengths than those of the individual basalts. Moreover, the mix of rocks produced CRF with a higher tensile strength than a single rock in general, even with a lower SiO_2 content. An increase in NF would increase the viscosity, which leads to difficulty in homogenization and an increased possibility of defects. Gutnikov et al. (2019) argued that if the increase in the content of glass-forming oxides (aluminum or silicon oxides) leads to increased strength, quartz fibers should have the maximum tensile strength. Although the role of SiO_2 seems to be the most fundamental compared to other oxides, there is no universal law for the effect of composition on tensile strength because the glass structure changes with composition as does the valence of certain oxides. The tensile strength of GF is influenced by a complex interplay of factors beyond just the content of glass-forming oxides. Local atomic arrangements and bonding characteristics, production stability and defects play a crucial role in determining the overall mechanical properties of the network. This complexity makes it challenging to predict strength solely based on composition, necessitating a more nuanced understanding of the structure–property relationships in CRF.

Al_2O_3, as a network mediator, plays a dual role in the tensile strength of CRF. Jung & Subramanian (1993) proposed that adding 2 wt% pure Al_2O_3 to the rock (initial 13.8 wt%) increased the tensile strength of bare CRF, while it decreased when the addition reached 3 wt%. Al reduced the non-bridging oxygen of the Si^{4+} tetrahedrons, whereas when the Al^{3+}: Na^+ ratio exceeded 1:1, it became an NM, weakening the glass network. Two types of ''flaws'' are proposed in Figure 11a, corresponding to the two peaks. Adding aluminum oxide might reduce the formation probability of the weaker flaw from A (no addition of Al_2O_3) to D with alumina addition 3wt%. Deák & Czigány (2009) and Ralph et al. (2019) reported that ceramic-like materials have a positive effect on the tensile strength, similar to the elastic modulus (Fig. 11b). Xing et al. (2019) explained that the role of Al depends on the molar ratio of $n(Al^{3+})/n(R^+/R^{2+})$ in the material, where R represents alkali and alkaline earth metals. Al^{3+} was considered as an NF to occupy the central position of the $[AlO_4]^{5-}$ tetrahedron when the ratio was less than 1.0 (Fig. 11c). Gutnikov et al. (2009) studied rocks with 10 to 24 wt% Al_2O_3, suggesting a constantly increased tensile strength with more Al_2O_3. The FT–IR spectra showed that the silicate glass contained a structure composed of three oxygen-sharing tetrahedrons, which increased the tensile strength. Kuzmin et al. (2017) observed that AI^{3+} exists in both fourfold and sixfold coordination in CRF through magic angle spinning (MAS–NMR), with Al^{IV} as an NF but $A1^{VI}$ NM.

FeO and Fe_2O_3 determine the physical and mechanical properties of CRFs, including their density, color, heat conduction, and temperature stability (Jamshaid & Mishra, 2016). Local crystallization can be regarded as 'defect,' which reduces tensile strength. Makhova (1968) found that the oxidation of iron determined the beginning of the crystallization, with pyroxenes crystallizing as centers. This effect was further researched, concluding that an increased Fe^{2+}/Fe^{3+} ratio decreased the spinel-like phase crystallization ability (Gutnikov et al., 2013). A higher value of Fe^{3+}/Σ Fe resulted in a smaller Weibull modulus, indicating a less uniform distribution of defects along the fiber length (Xing et al., 2019). Austin & Subramanian (1979) proposed that a reduction in Fe^{3+} content or drawing fibers in an inert or reducing atmosphere can improve the tensile strength. The reduction of iron oxidation was reported to slow down crystallization and reduce defects. Later research used treatments such as drawing fibers in an H_2/Ar atmosphere at 650–700 °C (Gutnikov et al., 2013), MnO_2 (oxidation), carbon powder (reduction), and citric acid (reduction) (Luo et al., 2019), which verified the positive linear relationship between the iron redox index ($IRI = Fe^{2+}/Fe_{total}$) and tensile strength (Fig. 11d). The figure also shows that the color of the RFs darkened with increasing IRI. Manylov et al. (2015) used a graphite crucible to conduct the basalt rock deferrization to lower the Fe content. The treated glass turned lighter in color than the original dark black glass (Fig. 11e). No significant improvement was found in the tensile strength of the resultant

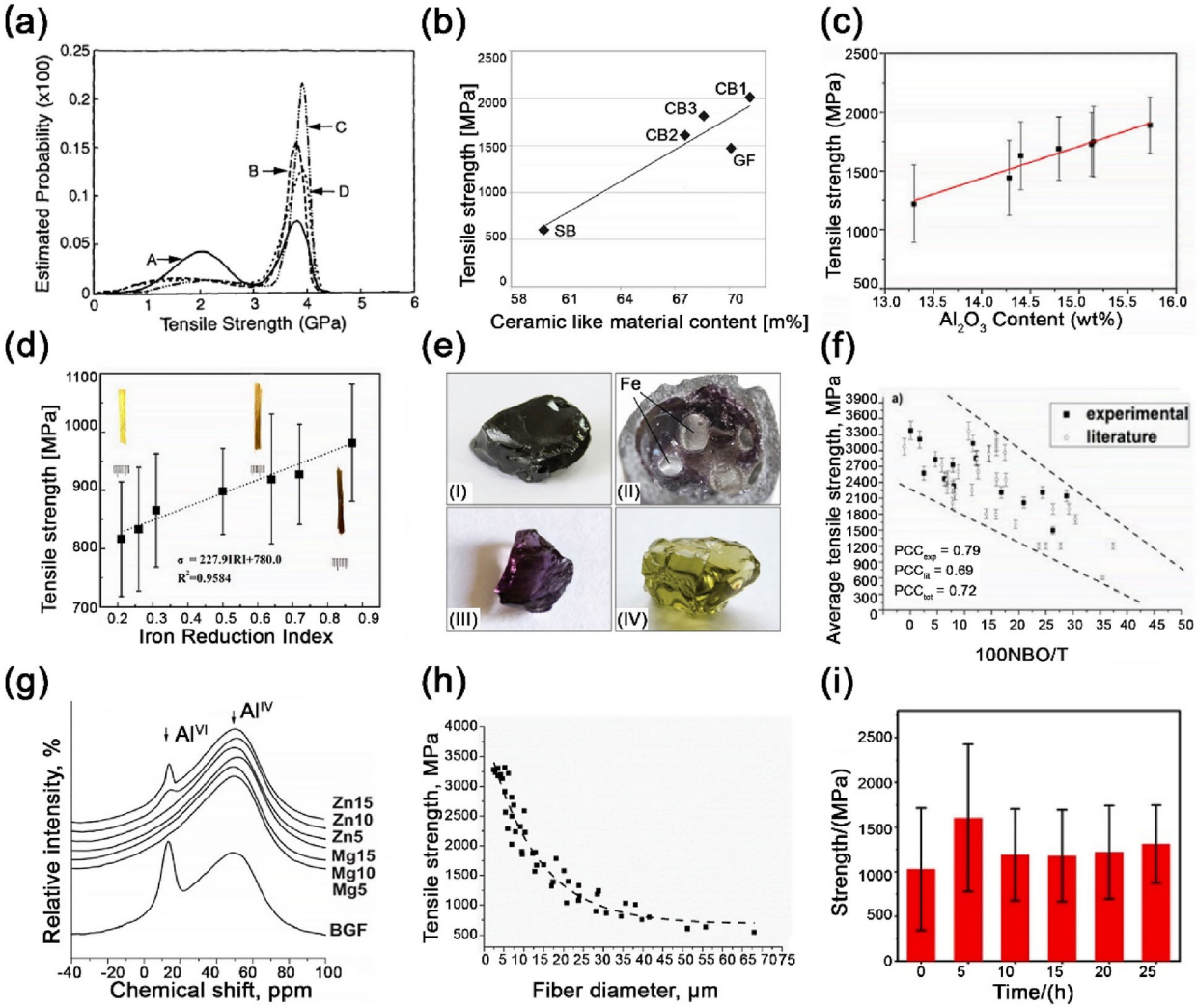

Figure 11. (**a**) Weibull distribution curves for fiber strengths at 22 mm GL; Al addition: A = none, B = 1 wt%, C = 2wt%, and D = 3wt% (Jung & Subramanian, 1993). (**b**) Correlation of ceramics (SiO_2 and Al_2O_3) content and tensile strength (Deák & Czigány, 2009). (**c**) Correlation between the Al_2O_3 content and tensile strength of single basalt fiber (Xing et al., 2019). (**d**) Tensile strength of basalt fiber samples under different deduction treatments (Luo et al., 2019). (**e**) (I) Original basalt glass; (II) iron sediment on the graphite crucible bottom; (III) reduced glass; (IV) deferrized glass after remelting (Manylov et al., 2015). (**f**) Dependence of filament tensile strength on the NBO/T parameter. (Gutnikov et al., 2019) (**g**) Al MAS NMR spectra for basaltic glass fibers with varying mole fractions of MgO and ZnO (Kuzmin et al., 2017). (**h**) Dependence of basalt fiber tensile strength on their diameter (Gutnikov & Lazoryak, 2019). (**i**) Tensile strength of basalt fibers prepared under different homogenization times (Yang et al., 2022).

CRF at room temperature, whereas a lower strength reduction was observed at 850 °C compared to the untreated CRF.

However, some researchers considered iron differently. Chen & Huang (2016) suggested that Fe_2O_3 is the main mediator, similar to Al_2O_3, while FeO is an NM, similar to alkali metals. Liu et al. (2020a) discussed the existence of Fe^{3+} in two states: $[FeO_4]$ tetrahedron and $[FeO_6]$ octahedron. When the rock contains a certain amount of alkali and alkaline-earth metals, Fe^{3+} accommodates $[SiO_4]$ tetrahedrons in the form of $[FeO_4]$ tetrahedrons and acts as NF. Fe^{3+} increased the melt viscosity and crystallization activation energy, resulting in improved tensile strength of the fibers. When glass lacks alkali and alkaline-earth metals, Fe^{3+} forms $[FeO_6]$ octahedrons as an NM. Chen et al. (2015) proposed the oxidation of ferrous to ferric as a pretreatment of rock, limiting the FeO percentage to less than 33.3% of the total iron oxides. The patent

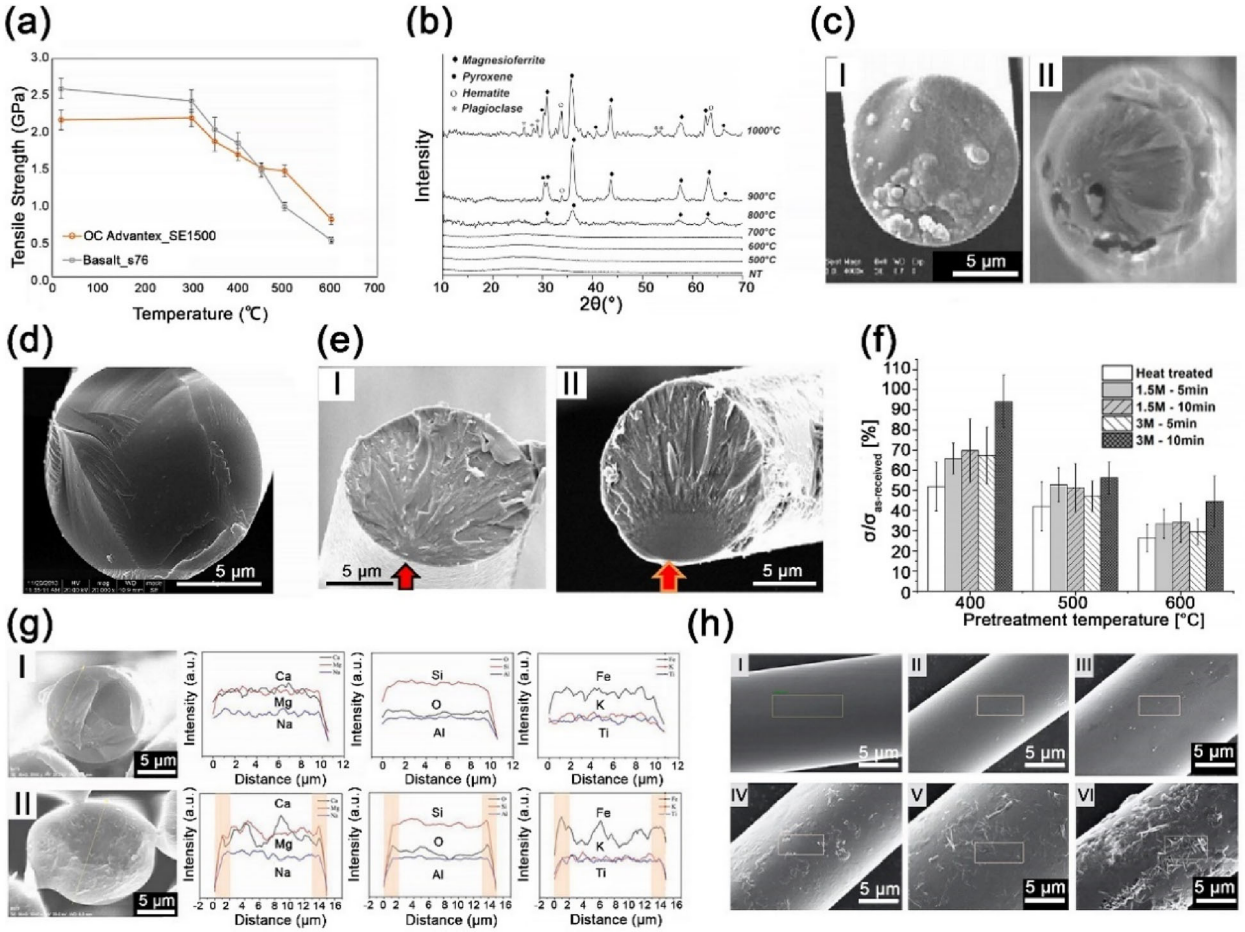

Figure 12. (**a**) Tensile strengths of epoxy compatible sized Advantex E-glass fiber and basalt fiber after bundle heat treatment for 25 minutes (Jenkins et al., 2015). (**b**) XRD patterns for BCF13 fibers heat treated in the temperature range 500 to 1000 °C for 1 h in air (Sarasini et al., 2018). (**c**) SEM micrographs of fractured planes of a basalt monofilament: (I) from Sabet et al (Sabet et al., 2015). (II) from Militký et al. (2002) (**d**) SEM images of bare RF on transverse section (Chen & Huang, 2016). (**e**) RF in (I) original condition and (II) exposure to 350 °C for 2 h. The arrow indicates the location of the pre-existing crack (Bhat et al., 2017). (**f**) Percentage of strength retention for RFs pretreated under different temperatures with NaOH treatment under different time and concentrations (Lilli, Sarasini, et al., 2020a, 2020b). (**g**) EDS charts of the elemental distribution over the fiber cross section of the raw RFF (I) and RFF-1000 °C (II) (Xing et al., 2022). (**h**) Surface morphology of RFs with different IRIs after heat treated at 600 °C; (I)IRI = 0.33 pristine, (II)IRI = 0.33, (III)IRI = 0.52, (IV)IRI = 0.64, (V) IRI = 0.74, and (VI) IRI = 1.00 (Wang et al., 2021).

claimed that Fe^{3+} improved the viscosity and contributed to better heat transfer of the melt with a lighter color, thus improving the CRF tensile strength. Luo et al. (2019) suggested that although the ferric ion was a NF, it was replaced by the much stronger NFs like Al^{3+} and Si^{4+} in reduction process. This was confirmed by the FT–IR results with an enhancement of absorption at approximately 756 cm^{-1}. Xing et al. (2019) proposed that Fe is an NF when the redox ratio of iron Fe^{3+}/Σ Fe > 0.5, and < 0.3 as NM. The debate lies in the trade-off between the compact network and homogenization, corresponding to the ''ideal'' material with stronger local bonding, more compact network structure, and a higher tensile strength, and the ''actual'' material containing defects, unhomogenized regions and crystals, leading to a lower tensile strength.

Alkali oxides, including CaO, Na_2O, and K_2O, are regarded as NMs. Although they are considered to loosen the network and decrease the CRF tensile strength (Meng et al., 2021), they could reduce the melt viscosity and decrease the temperature of fiber formation, thus contributing to better homogenization of the melt and eventually improving the tensile strength (Kuzmin et al., 2016). Chen et al. (2017b) suggested a small effect of Na_2O and K_2O on the

CRF tensile strength. Gutnikov et al. (2019) used the M_a and the NBO/T to predict the tensile strength of CRF using a linear function. The increase in alkaline earth and alkali ions depolymerized the glass structure with the formation of NBO. The PCCs of NBO/T and Ma with tensile strength were 0.79 and − 0.53, respectively (Fig. 11f). Si et al. (2021) observed using XRD and TEM that CaO changed the crystallization behavior of CRF by inhibiting spinel crystals and promoting pyroxene and plagioclase. The crystallization activation energy for spinel was calculated to increase from 270.08 to 427.08 KJ/mol, and the tensile strength increased by 13% with the addition of 3 wt% CaO.

The effect of MgO has been proposed differently in previous research. According to Morozov et al. (2001), elevated levels of CaO and MgO oxides in basalts could potentially result in enhanced crystallization. Chen & Huang (2016) considered TiO_2 and MgO as network intermediates, whereas Chen et al. (2017a) described them as NMs, both of which were not verified experimentally. Kuzmin et al. (2017) added 5 to 15 mol % MgO to the bare CRF, which led to a constant increase of tensile strength up to 43%. The observations under MAS–NMR and FT–IR spectroscopy suggested that MgO slightly decreased the degree of network polymerization. However, the authors mentioned that higher field strength ions, such as Mg^{2+}, resulted in the strongest bonds strengthening the glass. Mg was also assumed to change the coordination of Al from $A1^{VI}$ to Al^{IV} (Fig. 11g).

The effects of mineral components can be summarized as silicate structures. Chen et al. (2017b) proposed that quartz, orthoclase, and plagioclase were silicates with a three-dimensional frame structure, which formed a tight basalt glass network. Pyroxene (diopside and hypersthene) has a one-dimensional chain structure that forms a loose network. An increase in the frame structure element and a decrease in the chain structure element in the glass network structure may improve the tensile strength of the CRF. Similar to the debate mentioned above, the research team suggested that the ''dominate'' composition in the rock as AN series (quartz, orthoclase, and plagioclase anorthite, and albite) on the tensile strength was influenced by the production process, which led to the formation of defects and crystallization. A higher content of AN series led to a high melting temperature and viscosity, leading to difficulty in homogenization. This explained the low tensile strength of CRF with high content of NFs. (Chen et al., 2020). Gutnikov et al. (2021) quantified the phase component of 14 different rock samples, concluding that the tensile strength of the CRFs had no correlation with the content of framework, chain, and layered aluminosilicates. It may be influenced by the laboratory plant scheme, the tensile strength measurement methodology, the fiber diameter, and the melt temperature, which are variables in industrial and laboratory practice, above the theoretical explanation purely based on the material itself.

As mentioned, some studies suggested that low chemical composition variations have a minor effect on the tensile strength, whereas the effect comes more from the production, including the melt homogenization time, T_d, and r_0 (Dalinkevich et al., 2009; Jamshaid & Mishra, 2016). The fiber diameter r_0 based on Eq. 9 leads to different cooling conditions along the fiber cross section. A large diameter resulted in faster cooling on the surface and slower cooling in the fiber core, which may lead to crystallization. Fibers with a greater diameter should, on average, have a greater chance of having a large flaw and will therefore be weaker than thinner fibers (Sarasini et al., 2018). The study by Gutnikov & Lazoryak (2019) revealed that an increase in fiber diameter from 5 to 30 μm led to a sharp decrease in tensile strength (Fig. 11h). Although the fibers were produced in the same batch, the difference in performance was probably caused by the diameter difference and defects under different nozzles (Xing et al., 2019). One estimation is that the higher strength population in RFs is controlled by internal defects and the lower strength by mild surface flaws (Jung & Subramanian, 1993). Moreover, the fiber strength increased with increasing homogenization time when the homogenization time was 5 h (Fig. 11i) (Yang et al., 2022). When the degree of melt polymerization increased, the melt structure tended to stabilize along with the longer homogenization time, while the improvement was not obvious when the time exceeded 5 h. Crystals and flaws are typically categorized as defects, although a comprehensive definition of defects within an amorphous structure has not yet been established. It is a general barrier for amorphous materials, which hinders the conclusion of a structure–property relationship (Yang et al., 2021).

Although the heat resistance of CRF is claimed to be superior to that of CF and GF, it tends to crystallize when given sufficient external energy with an increase in temperature, which might reduce its

tensile strength with stress concentration in the inhomogeneous crystalized areas. Under heat treatment, the fiber underwent sizing decomposition, structural relaxation, and local crystallization. Sizing decomposition under low temperatures has been proven by researchers, while inconsistency occurs at a specific temperature. Jenkins et al. (2015) measured the weight loss of sized RF under heat treatment using TGA at around 200 °C. Förster et al. (2016) used atomic force microscopy (AFM) images and showed that the sizing remained after 450 °C with an increase in surface roughness. However, the TGA results showed an early removal of the sizing agent before 350 °C. The surface roughness and partial exposure of surface flaws may affect the strength drop after 300 °C (Fig. 12a). Researchers have proposed the existence of structural rearrangement with the relaxation of structural anisotropy and enthalpy due to high-temperature exposure, which is yet to be verified. Boutenel et al. (2020) suggested that there was an increase in the elastic modulus and density of the treated fiber, which might prove the structural rearrangement.

Crystallization occurs at high temperatures and follows a process similar to that of melting and fiber-drawing process, exhibiting a ''memory phenomenon.'' The XRD spectrum indicated the emergence of crystalline at approximately 750°C (Wang et al., 2012) to 800 °C (Fig. 12b) (Sarasini et al., 2018). The proposed process involved iron oxidation and magnetite formation at the beginning of crystal nucleation at 750 °C, followed by diopside (main phase) and anorthite (minor phase) at 900–1000 °C. Evidence from fractographic analysis under SEM from Sabet et al. (2015) and Militký et al. (2002) showed that the fracture occurred in different planes on the cross section. This suggests that defects were formed at various levels (Fig. 12c). For comparison, Figure 12d indicates a probably isotropic structure of the untreated bare CRF cross section (Chen & Huang, 2016). Bhat et al. (2017) observed the sized CRF before and after heating (Fig. 12e), which further proved that failure was always initiated at the surface (mirror region) and that the zone size increased with an increase in temperature (Sarasini et al., 2018). Lilli et al. (2020b) used acid and alkaline to treat heated CRF and obtained a recovery of the tensile strength (Fig. 12f), which also proved that more defects were present on the fiber surface. Xing et al. (2022) identified enrichment of Ca, Mg, and Fe on the fiber surface under heat treatment (Fig. 12g). This further explains how the components are transferred during the crystallization process. Contrary to the commonly proposed that local crystallinity will decrease the tensile strength of CRF, Wang et al. (2021) identified a CaO nanocrystalline layer on the surface of the fiber with a high iron reduction rate ($Fe^{2+}/\Sigma Fe$) (Fig. 12h). The crystal size increased with an increase in the iron reduction rate. These layers were suggested to increase the tensile strength at high temperatures, preventing the sintering of CRF.

Bare CRF usually undergoes basic sizing and lubricating processes to keep the filaments together, enhance the mechanical properties, and improve fiber–matrix adhesion (Mahltig & Kyosev, 2018). This coating mainly comprises organic materials involving a film former, coupling agent, lubricant, and sometimes other additives (Thomason & Adzima, 2001). The methods used to remove sizing include acetone (Xing et al., 2019) or heat treatment (Boutenel et al., 2020); however, the damage to the fiber after treatment is not certain, which would probably affect the later experimental results. As previously mentioned, the sizing effect on the yarn surface can affect the tensile strength. The study on sizing applications covers the majority of CRF research articles as it is the interface between the fiber and another matrix, especially in RFRC. Commonly used RFRC matrices include ceramics, concretes, and polymers. A rough surface can increase the inorganic bonding between the fiber and matrix, -which improves the performance of the composites. Studies conducted by Wei et al. (2011a, 2011b) employed the sol–gel technique to create an epoxy film coating approximately 400 nm thick, incorporating SiO_2 nanoparticles. Surface modification improves the mechanical properties of the fiber by acting as an adhesion to surface defects and increasing the surface roughness. Other surface modification methods include surface coupling agent modification, surface coating, nanoparticle loading, and etching (Wu et al., 2020). Kuzmin et al. (2016) studied the effects of Na_2O and Li_2O through ion exchange; they also added ZnO to CRF with an improvement of 47% in the tensile strength (Kuzmin et al., 2017).

The study of tensile strength involves chemical components, mineral components, production parameters, property changes under heat treatment, and the effect of sizing. The general debate lies in the trade-off between the compact network and defects on the tensile strength of CRF. As an amorphous material, the ''ordered'' microstructure like crystals are categorized as defects, while there

exist certain flow units with higher energy that can be ''defects.'' The flaws and scratches under production in macro-scale are also regarded as ''defects'' in the Griffith theory. The definition and categorization of defects are a general barrier apart from the network theory in the case of tensile strength compared to the elastic modulus. The distribution of defects is another key issue, as a homogenized distribution of crystals might reveal a compact structure, which would possibly improve the tensile strength. A localized crystallization, which is commonly seen in CRF, functions as a defect that would reduce the tensile strength. Crystallization under heat treatment has been comprehensively studied, while the proposed method of improving the tensile strength relies more on the surface sizing and treatment as the defects are found to initialize from the surface. The relationship between the tensile strength and elastic modulus is worth mentioning. The study of elastic modulus can be fundamental to the study of tensile strength, as the elastic modulus can be explored regardless of the defects at the macro-level, only considering the microstructure, including the network, local atom coordination, and bonding, whereas the tensile strength can be studied based on the elastic modulus and beyond, focusing on characterizing the defects under different levels.

CONCLUSIONS AND OUTLOOK

This review summarizes and clarifies the current theories, models, experimental approaches, and characterization methods. It investigates the parameters in different CRF production stages (rock screening, melting, cooling, and fiber drawing) and their impact on the mechanical properties of CRF, particularly on the tensile strength and elastic modulus. The limitations and debates regarding the results are highlighted. MD and ML have been proposed for future studies on the microstructure–property relationship of CRF.

As an overview of the research articles on CRF, tensile strength and heat resistance are the two main properties studied, while research on elastic modulus is minimal. The most studied aspects that affect CRF properties include fiber sizing and melting properties of basalt. Among the chemical components, the iron content has received the most attention from researchers. However, there is disagreement regarding its impact on CRF performance owing to its complex role in both the melting and fiber-forming processes. The mechanical properties of CRF are studied using two approaches: One follows the production process from the initial rock to melting, fiber drawing, and glass forming. The change in the microstructure was analyzed by considering the effect of each process. The other one starts from the end fiber, observing the fiber through characteristic methods and treatments, and explaining the structure–property relationship directly from the observed result.

The first approach includes diverse models because each production process has its own external conditions. In the melt stage, the continuous random network model with NF and NM explains the role of chemical components on viscosity, with more NF showing higher viscosity and corresponding tensile strength. The mineral components are based on the structure of the silicate tetrahedrons and the number of bridging oxygens in Q^n, with a denser structure contributing to a higher elastic modulus. In the fiber-forming stage, the balance of mass, force, energy, and momentum is used through numerical models with certain simplifications to analyze the stable fiber-drawing process. The transformation from basalt melt to glass is preliminarily explained through the TTT diagram, but the detailed microstructural changes under fast cooling remain unclear. To date, the fluid–structure interaction within material has not been investigated. Viscosity is a crucial parameter that affects homogenization, balances with the drawing force, and reflects the possible mechanical properties of the final CRF. The study of the change of microstructure from mineral crystals to the melt, and the short-, middle-, and long-range order of the formation of glass needs further explanation. Moreover, CRF is generally considered to be isotropic, similar to basalt glass; if the drawing and cooling processes affect the rearrangement of the microstructure, the structural difference between the fiber core and surface, and the effect of the asymmetrical radial temperature field is aspects worth studying. The advantage of this approach is the thorough understanding of the different stages of CRF formation, which clarifies the reasons for the ultimate fiber microstructure and properties. The difficulty lies in the connection between different stages, as they are all analyzed separately in individual studies.

In the second approach, the effects of the chemical components on the mechanical properties, including tensile strength and elastic modulus of

CRF, are directly explained through a continuous random network model. The presence of volume defects such as inter-fiber cracks and cavities, specifics of their distribution in the longitudinal and radial directions, and the presence of surface defects do not have a significant effect on altering the elasticity modulus of the fiber but produce a substantial decrease in the tensile strength. There is a general debate on the trade-off between the compact network and defects on the tensile strength of CRF. The study on elastic modulus can be the fundamental of the study on tensile strength, as the elastic modulus can be explored regardless of the defects in macro-level, only considering the microstructure including the network, local atom coordination and bonding, whereas the tensile strength can be studied based on elastic modulus and beyond, focusing on characterizing the defects under different levels. This approach offers a more direct understanding of the CRF structure, with less concern for the reasons for the corresponding property. It is more direct, but it would provide limited information about how to improve CRF properties from the rock sources or production settings compared to the first approach.

There are obvious limitations remaining in the methods used to study basaltic rocks and CRF. As the glass material is metastable, the theories for crystals and stable matter have limitations in explaining amorphous states. The theory explaining the monofilament glass is yet to be clarified, and the complicated composition of natural basalt rock makes the work more strenuous. Experimentally, the challenge lies in the in situ testing of fiber, which is difficult for certain procedures that cause permanent damage to the fiber. The effects of variations in rock composition make it difficult to isolate the influence of each factor in the study of this issue. As the experimental procedure was not standardized and the rock compositions used varied, the results in terms of specific data from different experiments could not be easily compared.

ML and MD have been used to study glass and amorphous alloys. MD simulation can compensate for the lack of experimental data, reduce the effects of experimental operation procedures, and provide more structure-based information, which is difficult to obtain experimentally. On the other hand, ML can reduce the computational cost required by MD and reflect the combined effect of different input features. Challenges in this approach lie in increasing the dimensions of the simulation so that the simulation result can be comparable to the experimental results. Moreover, the research should be based on a thorough understanding of the current research theory and experimental outcomes, which can guide the proposal of questions and apply PINN with physical theories under detailed cases, so that ML and MD can be applied to improve the validity of the model. The challenges and proposed future research directions in this review may help further research on high-performance CRF.

FUNDING

Open access funding provided by The Hong Kong Polytechnic University.

DECLARATIONS

COMPETING INTERESTS The authors declare no competing interest.

OPEN ACCESS

REFERENCES

Abd El-Moneim, A. (2001). Bond compression bulk modulus and Poisson's ratio of the polycomponent silicate glasses. *Materials Chemistry and Physics, 70*(3), 340–343.

Agrawal, A., & Choudhary, A. (2016). Perspective: Materials informatics and big data: Realization of the fourth paradigm of science in materials science. *APL Materials, 4*(5), 053208.

Al-Rousan, E. T., Khalid, H. R., & Rahman, M. K. (2023). Fresh, mechanical, and durability properties of basalt fiber-rein-

forced concrete (RFRC): A review. *Developments in the Built Environment, 14*, 100155.
Andreevskaya, G., & Plisko, T. (1963). Some physical properties of continuous basalt fibers. *Glass and Ceramics, 20*, 418–420.
Arrhenius, S. (1889). Quantitative relationship between the rate a reaction proceed and its temperature. *Journal of Physical Chemistry, 4*, 226–248.
Austin, H. F., & Subramanian, R. V. (1979). Method for forming basalt fibers with improved tensile strength. In: Google Patents.
Bauer, F., Kempf, M., Weiland, F., & Middendorf, P. (2018). Structure-property relationships of basalt fibers for high performance applications. *Composites Part B: Engineering, 145*, 121–128.
Bhat, T., Fortomaris, D., Kandare, E., & Mouritz, A. P. (2017). Properties of thermally recycled basalt fibres and basalt fibre composites. *Journal of Materials Science, 53*(3), 1933–1944.
Bottinga, Y., & Weill, D. F. (1972). The viscosity of magmatic silicate liquids; a model calculation. *American Journal of Science, 272*(5), 438–475.
Boutenel, F., Dusserre, G., & Cutard, T. (2020). Strength loss of basalt-based mineral fibers after thermal desizing. *Revue Des Composites Et Des Materiaux Avances-Journal of Composite and Advanced Materials, 30*(3–4), 115–122.
Butler, K. T., Davies, D. W., Cartwright, H., Isayev, O., & Walsh, A. (2018). Machine learning for molecular and materials science. *Nature, 559*(7715), 547–555.
Cao, B., Xie, Z., Xie, Z., Yu, K., Deng, X., Wang, X., Yang, Y., Zhong, L., & Wang, S, Ltd, S. S. N. M. I. D. C., & Ltd, S. a. T. B. I. C. (2019, August 23). CN210322058U - Liquid temperature detection equipment for all-electric melting kiln - Google Patents. https://patents.google.com/patent/CN210322058U/en?oq=CN210322058U (in Chinese).
Černý, M., Sucharda, Z., Glogar, P., Strachota, A., & Goliáš, V. (2011). Basalt and E-glass continuous fibers as reinforcement in thermally stable composites with partially pyrolysed polysiloxane matrix. In *Basalt: Types, Petrology and Uses* (pp. 146-158). https://www.scopus.com/inward/record.uri?eid=2-s2.0-84891999421&partnerID=40&md5=51d5e033388b5e7c881RFdefd9febbbd.
Chen, Z., Yuan, X., Huang, H., Xian, P., & Cao, B. & Ltd, S. a. T. B. I. C. (2015, December 8). *CN105366934A - Pretreatment method used for preparing continuous volcanic fiber raw materials - Google Patents.* https://patents.google.com/patent/CN105366934A/en?oq=CN+105366934a#patentCitations.
Chen, M., Liu, J., & Wu, Z. (2022). Effect of Fe_2O_3 concentration on the properties of basalt glasses. *Journal of Natural Fibers, 19*(2), 575–585.
Chen, X., Zhang, Y., Hui, D., Chen, M., & Wu, Z. (2017a). Study of melting properties of basalt based on their mineral components. *Composites Part B: Engineering, 116*, 53–60.
Chen, X., Zhang, Y., Huo, H., & Wu, Z. (2017b). Improving the tensile strength of continuous basalt fiber by mixing basalts. *Fibers and Polymers, 18*(9), 1796–1803.
Chen, X., Zhang, Y., Huo, H., & Wu, Z. (2020). Study of high tensile strength of natural continuous basalt fibers. *Journal of Natural Fibers, 17*(2), 214–222.
Chen, Z., & Huang, Y. (2016). Mechanical and interfacial properties of bare basalt fiber. *Journal of Adhesion Science and Technology, 30*(20), 2175–2187.
Ciarella, S., Khomenko, D., Berthier, L., Mocanu, F. C., Reichman, D. R., Scalliet, C., & Zamponi, F. (2023). Finding defects in glasses through machine learning. *Nature Commun, 14*(1), 4229.
Cooper, R. F., Fanselow, J. B., Weber, J. K. R., Merkley, D. R., & Poker, D. B. (1996). Dynamics of oxidation of a Fe^{2+}-bearing aluminosilicate (Basaltic) melt. *Science, 274*(5290), 1173–1176.
Cross, W., Iddings, J. P., Pirsson, L. V., & Washington, H. S. (1902). A quantitative chemico-mineralogical classification and nomenclature of igneous rocks. *The Journal of Geology, 10*(6), 555–690.
Dalinkevich, A. A., Gumargalieva, K. Z., Marakhovsky, S. S., & Soukhanov, A. V. (2009). Modern basalt fibrous materials and basalt fiber-based polymeric composites. *Journal of Natural Fibers, 6*(3), 248–271.
Deák, T., & Czigány, T. (2009). Chemical composition and mechanical properties of basalt and glass fibers: A comparison. *Textile Research Journal, 79*(7), 645–651.
Deringer, V. L., Bernstein, N., Bartok, A. P., Cliffe, M. J., Kerber, R. N., Marbella, L. E., Grey, C. P., Elliott, S. R., & Csanyi, G. (2018). Realistic atomistic structure of amorphous silicon from machine-learning-driven molecular dynamics. *Journal of Physical Chemistry Letters, 9*(11), 2879–2885.
Deringer, V. L., Bernstein, N., Csanyi, G., Ben Mahmoud, C., Ceriotti, M., Wilson, M., Drabold, D. A., & Elliott, S. R. (2021). Origins of structural and electronic transitions in disordered silicon. *Nature, 589*(7840), 59–64.
Dhand, V., Mittal, G., Rhee, K. Y., Park, S.-J., & Hui, D. (2015). A short review on basalt fiber reinforced polymer composites. *Composites Part B: Engineering, 73*, 166–180.
Dhé, P. (1923). Tipping Crucible for Basalt Furnaces (United States Patent No. 1462446). U. S. P. OFFICE. https://patents.google.com/patent/US1462446A/en.
Ding, L., Lu, R., Wang, L., Zheng, Q., Mauro, J. C., & Zhang, Z. (2023). Nanoindentation-induced evolution of atomic-level properties in silicate glass: Insights from molecular dynamics simulations. *Journal of the American Ceramic Society, 107*(3), 1448–1458.
Dou, H., Bai, J., Lu, H., Zhang, T., Kong, L., Bai, Z., & Li, W. (2023). Effect of TiO_2 on preparation condition, mechanical properties and alkali resistance of continuous basalt fibers. *Cement and Concrete Composites, 136*, 104861.
Dou, H., Wang, Y., Bai, J., Kong, L., Bai, Z., Li, H., Guo, Z., & Li, W. (2024). Effect of melt homogenization on the structure and properties of zirconium-rich basalt fibers. *Ceramics International, 50*(10), 16940–16949.
Dzhigiris, D. D., Makhova, M. F., Gorobinskaya, V. D., & Bombyr, L. N. (1983). Continuous basalt fiber. *Glass and Ceramics, 40*(9), 467–470.
EarthChem. (2023, January 26). EarthChem- *Access Geochemical Data.* EarthChem - Open Data for Geochemistry. Retrieved December 4, 2024, from https://www.earthchem.org/data-access/.
Ersoy, O., Aydar, E., & Çubukçu, H. E. (2021). Geochemical evaluation of suitability of central anatolian (turkey) volcanic rocks for rock fiber production. *Natural Resources Research, 30*(2), 1093–1104.
Ersoy, O., Aydar, E., Çubukçu, H. E., & Atalay, C. (2022). Differentiation index: A new proxy for determining suitability of volcanic rocks for production of different fiber types. *Natural Resources Research, 31*(1), 117–130.
Continuous Basalt & Glass Fibers and Applications - IBE. (2019, November 29). IBE. Retrieved December 04, 2024, from https://www.ibe.at/technologies/continuous-basalt-glass-fibers-and-applications/.
Fiore, V., Scalici, T., Di Bella, G., & Valenza, A. (2015). A review on basalt fibre and its composites. *Composites Part B: Engineering, 74*, 74–94.
Förster, T., Sommer, G. S., Mäder, E., & Scheffler, C. (2016). Surface, interphase and tensile properties of unsized, sized and heat treated basalt fibres. *IOP Conference Series Materials Science and Engineering, 139*, 012019.
Frankberg, E. J., Lambai, A., Zhang, J., Kalikka, J., Khakalo, S., Paladino, B., Cabrioli, M., Mathews, N. G., Salminen, T., Hokka, M., Akola, J., Kuronen, A., Levanen, E., Di Fonzo, F., & Mohanty, G. (2023). Exceptional microscale plasticity

in amorphous aluminum oxide at room temperature. *Advanced Materials, 35*(46), e2303142.
Fulcher, G. S. (1925). Analysis of recent measurements of the viscosity of glasses. *Journal of the American Ceramic Society, 8*(6), 339–355.
Galimzyanov, B. N., Doronina, M. A., & Mokshin, A. V. (2023). Machine learning-based prediction of elastic properties of amorphous metal alloys. *Physica A: Statistical Mechanics and its Applications, 617*, 128678.
Griffith A. A. (1921). The Phenomena of Rupture and Flow in Solids. *Philos Trans R Soc A Math Phys Eng Sci*, 163–198.
Guo, Z., Lu, D., Yan, Y., Hu, S., Liu, R., Tan, G., Sun, N., Jiang, W., Liu, L., & Chen, Y. (2022b). Extending the limit of molecular dynamics with ab initio accuracy to 10 billion atoms. Proceedings of the 27th ACM SIGPLAN Symposium on Principles and Practice of Parallel Programming, 205–218. https://doi.org/10.1145/3503221.3508425.
Guo, Z., Xing, D., & Ma, P. (2023). Study on the Influence of Chemical Composition and Fiber Forming Process on the Atomic Structure of Basalt Fiber. International Commission on Glass, 276. https://vbn.aau.dk/ws/portalfiles/portal/631591825/ICG2023-Abstract_1_.pdf.
Guo, Z. S., Xing, D., Xi, X. Y., Liang, C. G., Hao, B., Zeng, X., Tang, H., Chen, H., Yin, W., Zhang, P., Zhou, K., Zheng, Q., & Ma, P. C. (2024). Production of Martian fiber by in-situ resource utilization strategy. *iScience, 27*(8), 110408.
Guo, Z. S., Xing, D., Xi, X. Y., Yue, X., Liang, C. G., Hao, B., Zheng, Q., Gutnikov, S. I., Lazoryak, B. I., & Ma, P.-C. (2022a). Production of fibres from lunar soil: Feasibility, applicability and future perspectives. *Advanced Fiber Materials, 4*(5), 923–937.
Gur'ev, V. V., Neproshin, E. I., & Mostovoi, G. E. (2001). The effect of basalt fiber production technology on mechanical properties of fiber. *Glass and Ceramics, 58*(1/2), 62–65.
Gutnikov, S. I., & Lazoryak, B. I. (2019). Effect of nozzle diameter on basalt continuous fiber properties. *Fibers, 7*(7), 65.
Gutnikov, S. I., Malakho, A. P., Lazoryak, B. I., & Loginov, V. S. (2009). Influence of alumina on the properties of continuous basalt fibers. *Russian Journal of Inorganic Chemistry, 54*(2), 191–196.
Gutnikov, S. I., Manylov, M. S., Lipatov, Y. V., Lazoryak, B. I., & Pokholok, K. V. (2013). Effect of the reduction treatment on the basalt continuous fiber crystallization properties. *Journal of Non-Crystalline Solids, 368*, 45–50.
Gutnikov, S. I., Popov, S. S., Efremov, V. A., Ma, P.-C., & Lazoryak, B. I. (2021). Correlation of phase composition, structure, and mechanical properties of natural basalt continuous fibers. *Natural Resources Research, 30*(2), 1105–1119.
Gutnikov, S. I., Zhukovskaya, S. E., Popov, S. S., & Lazoryak, B. I. (2019). Correlation of the chemical composition, structure and mechanical properties of basalt continuous fibers. *AIMS Materials Science, 6*(5), 806–832.
Han, Q. Y., Xi, X. Y., Ma, Y., Wang, X., Xing, D., & Ma, P. C. (2024). Predicting the viscosity of basalt melt by data-driven and interpretable machine learning. *Journal of Non-Crystalline Solids, 648*, 123302.
Hu, Y. J., Zhao, G., Zhang, M., Bin, B., Del Rose, T., Zhao, Q., Zu, Q., Chen, Y., Sun, X., de Jong, M., & Qi, L. (2020). Predicting densities and elastic moduli of SiO2-based glasses by machine learning. *npj Computational Materials, 6*(1), 25.
Ivanitskii, S. G., & Gorbachev, G. F. (2011). Continuous basalt fibers: production aspects and simulation of forming processes. I. State of the art in continuous basalt fiber technologies. *Powder Metallurgy and Metal Ceramics, 50*(3–4), 125–129.
Iwamori, H., & Nakamura, H. (2015). Isotopic heterogeneity of oceanic, arc and continental basalts and its implications for mantle dynamics. *Gondwana Research, 27*(3), 1131–1152.
Jamshaid, H. (2017). Basalt fiber and its applications. *Journal of Textile Engineering & Fashion Technology, 1*(6), 41.
Jamshaid, H., & Mishra, R. (2016). A green material from rock: basalt fiber – A review. *The Journal of The Textile Institute, 107*(7), 923–937.
Jenkins, P., Mendez, S. R., Rodriguez, E., Yang, L., & Thomason, J. (2015). Investigation of the strength of thermally conditioned basalt and e-glass fibres. https://pureportal.strath.ac.uk/files/43287374/Jenkins_etal_ICCM20_2015_Investigation_strength_thermally_conditioned_basalt_and_e_glass_fibres.pdf.
Johannesson, B., Sigfusson, T. I., & Franzson, H. (2019). Suitability of Icelandic basalt for production of continuous fibres. *Applied Earth Science, 128*(3), 73–78.
Jung, T., & Subramanian, R. V. (1993). Strengthening of basalt fiber by alumina addition. *Scripta Metallurgica et Materialia, 28*(4), 527–532.
Kamane, S. K., Patil, N. K., & Patagundi, B. R. (2021). Use of artificial neural network to predict the bending behavior of steel I beam externally attached with FRP sheets. *Materials Today: Proceedings, 39*, 17–21.
Kavya, B. R., Sureshchandra, H. S., Prashantha, S. J., & Shrikanth, A. S. (2022). Prediction of mechanical properties of glass and basalt fiber reinforced concrete using ANN. *Asian Journal of Civil Engineering, 23*(6), 877–886.
Khudyakova, L. I., Buyantuev, S. L., & Buyantuev, V. T. (2020). Basalts of the Republic of Buryatia and their suitability for obtaining mineral fibres. *IOP Conference Series: Materials Science and Engineering*, *962*(2). https://doi.org/10.1088/1757-899x/962/2/022032.
Kim, J. S., Lim, J. H., & Huh, Y. (2013). Melt-spinning basalt fibers based on dielectric heating and steady-state process characteristics. *Fibers and Polymers, 14*(7), 1148–1156.
Kim, Y., & Oh, H. (2021). Comparison between Multiple regression analysis, polynomial regression analysis, and an artificial neural network for tensile strength prediction of RFRP and GFRP. *Materials (Basel), 14*(17), 4861.
Kobayashi, K., Okumura, M., Nakamura, H., Itakura, M., Machida, M., Urata, S., & Suzuya, K. (2023). Machine learning molecular dynamics reveals the structural origin of the first sharp diffraction peak in high-density silica glasses. *Science and Reports, 13*(1), 18721.
Krenev, V. A., Fomichev, S. V., Pechenkina, E. N., Alikhanyan, A. S., & Voshkin, A. A. (2022). Effect of technological parameters on the formation of igneous rock melts (for gabbro used as an example) [Article]. *Theoretical Foundations of Chemical Engineering, 56*(4), 572–577.
Krenev, V. A., Kondakov, D. F., Pechenkina, E. N., & Fomichev, S. V. (2020). Modification of the composition of gabbro-basalt raw materials during melting in an oxidizing, inert, or reducing atmosphere [Article]. *Glass and Ceramics (English translation of Steklo i Keramika), 76*(11–12), 432–435.
Kuzmin, K. L., Gutnikov, S. I., Zhukovskaya, E. S., & Lazoryak, B. I. (2017). Basaltic glass fibers with advanced mechanical properties. *Journal of Non-Crystalline Solids, 476*, 144–150.
Kuzmin, K. L., Zhukovskaya, E. S., Gutnikov, S. I., Pavlov, Y. V., & Lazoryak, B. I. (2016). Effects of ion exchange on the mechanical properties of basaltic glass fibers. *International Journal of Applied Glass Science, 7*(1), 118–127.
LaDouceur, B. O., McCanta, M., Sharma, B., Sarabia, G., Dunn, N. E., & Darby Dyar, M. (2024). Predicting silicate glass geochemistry using Raman spectroscopy and supervised machine learning: partial least square applications to amorphous Raman spectra. *Applied Spectroscopy, 78*(5), 456–476.
Lamb, J. (1978). Viscoelasticity and lubrication: a review of liquid properties. *Journal of Rheology, 22*(4), 317–347.
Li, H., Lin, J., Zhao, D., Shi, G., Wu, H., Wei, T., Li, D., & Zhang, J. (2022). A RFRC compressive strength prediction method via kernel extreme learning machine-genetic algorithm. *Construction and Building Materials, 344*, 128076.
Lilli, M., Rossi, E., Tirillò, J., Sarasini, F., Di Fausto, L., Valente, T., González, C., Fernández, A., Lopes, C. S., Moscatelli, R.,

Bemporad, E., & Sebastiani, M. (2020a). Quantitative multiscale characterization of single basalt fibres: Insights into strength loss mechanisms after thermal conditioning. *Materials Science and Engineering: A, 797*, 139963.
Lilli, M., Sarasini, F., Fausto, L. D., González, C., Fernández, A., Lopes, C. S., & Tirillò, J. (2020b). Chemical regeneration of thermally conditioned basalt fibres. *Applied Sciences, 10*(19), 6674.
Liu, C., Zhang, H., Guo, L., Yuan, Z., Wang, D., Li, H., Jiang, L., & Yang, C. (2023). Preparation of continuous silicate fiber: Comparison of natural basalt and artificial stimulant with the same chemical composition. *Natural Resources Research, 32*(4), 1549–1558.
Liu, H., Shi, Y., Youngman, R. E., & Huang, L. (2024). Role of densification in deformation behaviors of model metallic glasses under 3-D nanoindentation studied in molecular dynamics simulation. *Journal of Non-Crystalline Solids, 638*, 123071.
Liu, J., Chang, Z., Wang, L., Xu, J., Kuang, R., & Wu, Z. (2020a). Exploration of basalt glasses as high-temperature sensible heat storage materials. *ACS Omega, 5*(30), 19236–19246.
Liu, J., Chen, M., Yang, J., & Wu, Z. (2020b). Study on mechanical properties of basalt fibers superior to E-glass fibers. *Journal of Natural Fibers, 19*(3), 882–894.
Liu, J., Yang, J., Chen, M., Lei, L., & Wu, Z. (2018). Effect of SiO_2, $Al2O_3$ on heat resistance of basalt fiber. *Thermochimica Acta, 660*, 56–60.
Luo, L., Zhang, Q., Wang, Q., Xiao, J., Liu, J., Ding, L., & Jiang, W. (2019). Effect of the iron reduction index on the mechanical and chemical properties of continuous basalt fiber. *Materials (Basel), 12*(15), 2472.
Magnien, V., Neuville, D. R., Cormier, L., Roux, J., Hazemann, J. L., de Ligny, D., Pascarelli, S., Vickridge, I., Pinet, O., & Richet, P. (2008). Kinetics and mechanisms of iron redox reactions in silicate melts: The effects of temperature and alkali cations. *Geochimica et Cosmochimica Acta, 72*(8), 2157–2168.
Mahltig, B., & Kyosev, Y. (2018). *Inorganic and composite fibers: production, properties, and applications*.
Makhova, M. (1968). Crystallization of basalt fibers. *Glass and Ceramics, 25*(11), 672–674.
Makhova, M. F., Gorbachev, G. F., Bocharova, I. N., Kovalenko, V. G., & Pipko, A. K. (1984). Production of superfine fibers from molten rocks. *Glass and Ceramics, 41*(8), 341–344.
Makhova, M. F., Sergeev, V. P., Zaidlin, E. B., & Khan, B. K. (1990). Interrelationship between the viscosity of melts and the composition of rocks in glass fiber fabrication. *Glass and Ceramics, 47*(10), 393–397.
Makishima, A., & Mackenzie, J. D. (1973). Direct calculation of Young's modulus of glass. *Journal of Non-Crystalline Solids, 12*(1), 35–45.
Makishima, A., & Mackenzie, J. D. (1975). Calculation of bulk modulus, shear modulus and Poisson's ratio of glass. *Journal of Non-Crystalline Solids, 17*(2), 147–157.
Manylov, M. S., Gutnikov, S. I., Lipatov, Y. V., Malakho, A. P., & Lazoryak, B. I. (2015). Effect of deferrization on continuous basalt fiber properties. *Mendeleev Communications, 25*(5), 386–388.
Martinez, L. M., & Angell, C. A. (2001). A thermodynamic connection to the fragility of glass-forming liquids. *Nature, 410*(6829), 663–667.
Meng, Y., Liu, J., Xia, Y., Liang, W., Ran, Q., & Xie, Z. (2021). Preparation and characterization of continuous basalt fibre with high tensile strength. *Ceramics International, 47*(9), 12410–12415.
Metal, Plastic, and Ceramic Search Index. (n.d.). Retrieved December 4, 2024, from https://www.matweb.com/search/MaterialGroupSearch.aspx.
Milardovich, D., Jech, M., Waldhoer, D., El-Sayed, A.-M. B., & Grasser, T. (2021). *Machine Learning Prediction of Defect Structures in Amorphous Silicon Dioxide* ESSDERC 2021 - IEEE 51st European Solid-State Device Research Conference (ESSDERC),.
Militky, J., & Kovacic, V. (1996). Ultimate mechanical properties of basalt filaments. *Textile Research Journal, 66*(4), 225–229.
Militký, J., Kovačič, V., & Rubnerová, J. (2002). Influence of thermal treatment on tensile failure of basalt fibers. *Engineering fracture mechanics, 69*(9), 1025–1033.
Morozov, N. N., Bakunov, V. S., Morozov, E. N., Aslanova, L. G., Granovskii, P. A., Prokshin, V. V., & Zemlyanitsyn, A. A. (2001). Materials based on basalts from the European North of Russia. *Glass and Ceramics, 58*(3–4), 100–104.
Morse, S. A. (1980). *Basalts and phase diagrams: an introduction to the quantitative use of phase diagrams in igneous petrology*. Springer.
Myasnikov, A., & Aslanova, M. (1965). Choice of basalt rock composition for producing fibers for various purposes. *Glass and Ceramics, 22*(3), 156–159.
Mysovsky, A. S., & Paklin, A. S. (2023). Molecular dynamics modeling of sio_2 melts and glass formation processes. *Glass Physics and Chemistry, 49*(3), 269–280.
Najjar, I. M. R., Sadoun, A. M., Abd Elaziz, M., Abdallah, A. W., Fathy, A., & Elsheikh, A. H. (2022). Predicting kerf quality characteristics in laser cutting of basalt fibers reinforced polymer composites using neural network and chimp optimization. *Alexandria Engineering Journal, 61*(12), 11005–11018.
Novitskii, A. G., & Efremov, M. V. (2013). Technological aspects of the suitability of rocks from different deposits for the production of continuous basalt fiber. *Glass and Ceramics, 69*(11–12), 409–412.
Osnos, S. (2016). Present and future of basalt fibre technology, manufacturing and market development. *JEC Composites magazine, 53*(108), 15–18.
Pavlyukevich, Y. G., Papko, L. F., Kravchuk, A. P., Larionov, P. S., & Yanson, S. Y. (2023). Influence of modifiers on the properties of basalt glasses and melts. *Glass and Ceramics, 80*(5–6), 227–232.
Pisciotta, A., Perevozchikov, B. V., Osovetsky, B. M., Menshikova, E. A., & Kazymov, K. P. (2014). Quality assessment of melanocratic basalt for mineral fiber product, southern Urals. *Russia. Natural Resources Research, 24*(3), 329–337.
Rahman, S. K., & Al-Ameri, R. (2021). Experimental investigation and artificial neural network based prediction of bond strength in self-compacting geopolymer concrete reinforced with basalt FRP bars. *Applied Sciences, 11*(11), 4889.
Rahman, S. K., & Al-Ameri, R. (2022). Experimental and artificial neural network-based study on the sorptivity characteristics of geopolymer concrete with recycled cementitious materials and basalt fibres. *Recycling, 7*(4), 55.
Rai, M., & Mountjoy, G. (2014). Molecular dynamics modelling of the structure of barium silicate glasses $BaO–SiO_2$. *Journal of Non-Crystalline Solids, 401*, 159–163.
Ralph, C., Lemoine, P., Summerscales, J., Archer, E., & McIlhagger, A. (2019). Relationships among the chemical, mechanical and geometrical properties of basalt fibers. *Textile Research Journal, 89*(15), 3056–3066.
Rocherulle, J., Ecolivet, C., Poulain, M., Verdier, P., & Laurent, Y. (1989). Elastic moduli of oxynitride glasses. *Journal of Non-Crystalline Solids, 108*(2), 187–193.
Rouxel, T. (2006). Elastic properties of glasses: A multiscale approach. *Comptes Rendus Mécanique, 334*(12), 743–753.
Rouxel, T. (2007). Elastic properties and short-to medium-range order in glasses. *Journal of the American Ceramic Society, 90*(10), 3019–3039.
Sabet, S., Akhlaghi, F., & Eslami-Farsani, R. (2015). The effect of thermal treatment on tensile properties of basalt fibers. *J Ceram Sci Tech, 6*(3), 245.

Sarasini, F., Tirillò, J., & Seghini, M. C. (2018). Influence of thermal conditioning on tensile behaviour of single basalt fibres. *Composites Part B: Engineering, 132*, 77–86.

Schreiber, E., Anderson, O., & Soga, N. (1973). *Elastic constants and their measurement*.

Self, S., Schmidt, A., & Mather, T. A. (2014). Emplacement characteristics, time scales, and volcanic gas release rates of continental flood basalt eruptions on Earth. *In Volcanism, Impacts, and Mass Extinctions: Causes and Effects*. https://doi.org/10.1130/2014.2505(16).

Shebanov, M. S. (2022). Maxwell model parameters for single filaments of aramid, glass, and basalt fibers. *Fibre Chemistry, 54*(1), 49–50.

Shi, J., Jiang, C., Zhai, Y., Qiu, Y., Shi, H., Li, J., Zhu, S., & Li, S. (2024). Phase equilibria of SiO_2–Al_2O_3–Fe_3O_{4-5} wt.% CaO system at 1400 °C in air relevant to the production of continuous basalt fibers: Emphasis on spinel solid solution phase. *Ceramics International, 50*(19), 35397–35404.

Si, J., Wang, Z., Li, J., Zuo, C., Zhang, P., Wei, C., Wang, J., Li, W., & Miao, S. (2021). Effects of CaO added to raw basalt on producing continuous basalt fibers and their mechanical properties. *Journal of Non-Crystalline Solids, 568*, 120941.

Sokolinskaya, M., Zabava, L., Tsybulya, T., & Medvedev, A. (1991). Strength properties of basalt fibers. *Glass and Ceramics, 48*, 435–437.

Sutera, S. P., & Skalak, R. (1993). The history of poiseuille's law. *Annual Review of Fluid Mechanics, 25*(1), 1–20.

Tatarintseva, O. S., & Khodakova, N. N. (2010). Obtaining basaltic continuous and staple fibers from rocks in Krasnodar Krai. *Glass and Ceramics, 67*(5–6), 165–168.

Tatarintseva, O. S., Khodakova, N. N., & Uglova, T. K. (2012). Dependence of the viscosity of basalt melts on the chemical composition of the initial mineral material. *Glass and Ceramics, 68*(9–10), 323–326.

Thomason, J. L., & Adzima, L. J. (2001). Sizing up the interphase: an insider's guide to the science of sizing. *Composites Part A: Applied Science and Manufacturing, 32*(3–4), 313–321.

Uhlmann, D. R. (1972). A kinetic treatment of glass formation. *Journal of Non-Crystalline Solids, 7*(4), 337–348.

Umar, S. A., & Ibrahim, G. G. (2020). Theoretical elastic moduli of TeO_2 – B_2O_3 – SiO_2 glasses. *EDUCATUM Journal Of Science, Mathematics And Technology, 7*(2), 18–30.

Vasil'eva, A. A., Kychkin, A. K., Anan'eva, E. S., & Lebedev, M. P. (2014). Investigation into the properties of basalt of the Vasil'evskoe deposit in Yakutia as the raw material for obtaining continuous fibers. *Theoretical foundations of chemical engineering, 48*, 667–670.

Vinay, S. S., Sanjay, M. R., Siengchin, S., & Venkatesh, C. V. (2022). Basalt fiber reinforced polymer composites filled with nano fillers: A short review. *Materials Today: Proceedings, 52*, 2460–2466.

Vogel, H. (1921). Das temperaturabhangigkeitsgesetz der viskositat von flussigkeiten. *Physikalishce Zeitschrift, 22*, 645–646.

Wang, L. (2021). *Study on effect of basalt fiber component on elastic modulus* Southeast University.

Wang, W. (2023). *Amorphous matter, the fourth conventional matter*. (in Chinese).

Wang, N., Hou, S., & Jin, H. Y. (2012). Crystallization behavior of heat-treated basalt fiber. *Advanced Materials Research, 560–561*, 3–7.

Wang, Q., Zhang, Q., Luo, L., Yan, T., Liu, J., Ding, L., & Jiang, W. (2021). Effects of high-temperature treatment and iron reduction index on tensile strength of basalt continuous fiber. *Journal of Non-Crystalline Solids, 564*, 120836.

Wang, W. H. (2005). Elastic moduli and behaviors of metallic glasses. *Journal of Non-Crystalline Solids, 351*(16–17), 1481–1485.

Wang, X. M., Kan, Q. H., Petru, M., & Kang, G. Z. (2024). Study on the composition-property relationships of basalt fibers based on symbolic regression and physics-informed neural network. *Composites Part a-Applied Science and Manufacturing, 185*, 108324.

Wei, B., Cao, H., & Song, S. (2011a). Surface modification and characterization of basalt fibers with hybrid sizings. *Composites Part A: Applied Science and Manufacturing, 42*(1), 22–29.

Wei, B., Song, S., & Cao, H. (2011b). Strengthening of basalt fibers with nano-SiO_2–epoxy composite coating. *Materials & Design, 32*(8–9), 4180–4186.

Weibull, W. (1951). A statistical distribution function of wide applicability. *Journal of Applied Mechanics, 18*(3), 293–297. https://doi.org/10.1115/1.4010337.

Xing, D. (2020). *Factors governing the mechanical properties of basalt fiber* University of Chinese Academy of Sciences.

Xing, D., Chang, C., Xi, X.-Y., Hao, B., Zheng, Q., Gutnikov, S. I., Lazoryak, B. I., & Ma, P.-C. (2022). Morphologies and mechanical properties of basalt fibre processed at elevated temperature. *Journal of Non-Crystalline Solids, 582*, 121439.

Xing, D., Xi, X.-Y., & Ma, P.-C. (2019). Factors governing the tensile strength of basalt fibre. *Composites Part A: Applied Science and Manufacturing, 119*, 127–133.

Xu, X., Niu, Y., Li, W., Dong, Y., Yang, Z., & Yu, X. (2024). Iron series fibers composition design model. *Materials Today Communications, 40*, 109515.

Yan, Q. Y., & Yan, Q. S. (2004). Numerical simulation of the viscosity flow process in the region of formation of basalt fibre. *Glass Technology, 45*(5), 227–232.

Yang, C. C., Liu, Z., Tong, X. C., Guo, L., Miao, S. T., Jiang, L. T., Li, Y., Li, H. C., & Liu, C. J. (2022). Effects of raw material homogenization on the structure of basalt melt and performance of fibers. *Ceramics International, 48*(9), 11998–12005.

Yang, K., Xu, X., Yang, B., Cook, B., Ramos, H., Krishnan, N. M. A., Smedskjaer, M. M., Hoover, C., & Bauchy, M. (2019). Predicting the young's modulus of silicate glasses using high-throughput molecular dynamics simulations and machine learning. *Scientific Reports, 9*(1), 8739.

Yang, Z. Y., Wei, D., Zaccone, A., & Wang, Y. J. (2021). Machine-learning integrated glassy defect from an intricate configurational-thermodynamic-dynamic space. *Physical Review B, 104*(6), 064108.

Yue, Y., & Zheng, Q. (2017). Fiber spinnability of glass melts. *International Journal of Applied Glass Science, 8*(1), 37–47.

Zachariasen, W. H. (1932). The atomic arrangement in glass. *Journal of the American Chemical Society, 54*(10), 3841–3851.

Zallen, R. (1983). *The Physics of Amorphous Solids*. https://doi.org/10.1002/3527602798.

Zhang, Y. (2009). *Geochemical Kinetics* https://doi.org/10.1063/1.3226771.

Zhang, L., Yang, L., Lai, C., Fu, D., Lin, J., Hou, H., Zhao, Y., Zhang, Z., Bu, C., & Zheng, X. (2023). Prediction of tensile strength of basalt continuous fiber from chemical composition using machine learning models. *Polymer Composites, 44*(10), 6634–6645.

Zhang, S., Hou, Y., Guo, J., Zhou, H., & Lv, X. (2024). Flowability and structural evolution of CaO-SiO_2-MgO-Al_2O_3 slag with varying MgO/CaO ratios: Experiments and MD simulations. *Journal of Non-Crystalline Solids, 634*, 122979.

Zhang, X.-L., Kou, J., Sun, C.-B., Zhang, R.-Y., Su, M., & Li, S.-F. (2021). Mineralogical characterization of copper sulfide tailings using automated mineral liberation analysis: A case study of the Chambishi Copper Mine tailings. *International Journal of Minerals, Metallurgy and Materials, 28*(6), 944–955.

Zhishen, Wu., Wang, X., Liu, J., & Chen, X. (2020). Mineral fibres. *Handbook of Natural Fibres* (pp. 433–502). Elsevier. https://doi.org/10.1016/B978-0-12-818398-4.00015-3.